NASA Technical Paper 3473

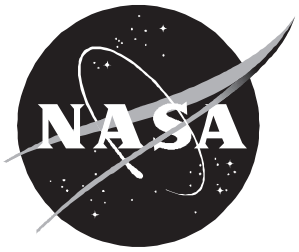

Performance Study of Galactic Cosmic Ray Shield Materials

Myung-Hee Y. Kim, John W. Wilson, Sheila A. Thibeault, John E. Nealy, Francis F. Badavi, and Richard L. Kiefer

November 1994

NASA Technical Paper 3473

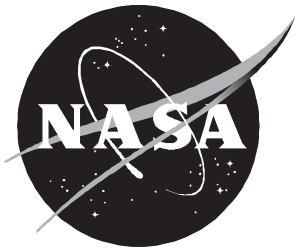

Performance Study of Galactic Cosmic Ray Shield Materials

Myung-Hee Y. Kim
College of William and Mary • Williamsburg, Virginia

John W. Wilson, Sheila A. Thibeault, and John E. Nealy
Langley Research Center • Hampton, Virginia

Francis F. Badavi
Christopher Newport University • Newport News, Virginia

Richard L. Kiefer
College of William and Mary • Williamsburg, Virginia

National Aeronautics and Space Administration
Langley Research Center • Hampton, Virginia 23681-0001

November 1994

The use of trademarks or names of manufacturers in this report is for accurate reporting and does not constitute an official endorsement, either expressed or implied, of such products or manufacturers by the National Aeronautics and Space Administration.

This publication is available from the following sources:

NASA Center for AeroSpace Information
800 Elkridge Landing Road
Linthicum Heights, MD 21090-2934
(301) 621-0390

National Technical Information Service (NTIS)
5285 Port Royal Road
Springfield, VA 22161-2171
(703) 487-4650

Summary

The space program is faced with two difficult radiation protection issues for future long-term operations. First, retrofit of shield material or conservatism in shield design is prohibitively expensive and often impossible. Second, shielding from the cosmic heavy ions is faced with limited knowledge on the physical properties and biological responses of these radiations. The current status of space shielding technology and its impact on radiation health is discussed herein in terms of conventional protection practice and a test biological response model. The impact of biological response on the selection of optimum materials for cosmic ray shielding is presented in terms of the transmission characteristics of the shield material. The transmission properties are, in turn, related to the nuclear cross sections of the cosmic heavy ions, for which an inadequate experimental database exists. Clearly, these physical and biological issues must be resolved before an adequate shield design can be defined.

The choice of structural materials composition is a means of reducing astronaut exposure risk from space radiations in future NASA missions. The use of a performance index for shield materials related to the change in biological protection at constant shield mass and varying shield composition indicates performance indices up to a factor of 20. Although the systematics of nuclear cross sections are able to demonstrate the relation of exposure risk to shield-material composition, the current uncertainty in nuclear cross sections will not allow an accurate evaluation of risk reduction. Even so, the unique role of hydrogenous materials used as high-performance shields is clear. Shinn et al. suggested that polyethylene with its short nuclear absorption lengths is an effective shield material in spite of the favoring of massive projectile fragments, and this is demonstrated herein for monoenergetic ion beams. This paper presents a theoretical study of risk-related factors and a pilot experiment to study the effectiveness of choice of shield materials to reduce the risk in space operations.

Introduction

In the past exploratory manned space missions lasting up to several weeks, only the more intense sources of space radiation, such as solar cosmic rays and trapped radiations, were considered to be the primary radiation hazards. The principal radiation protection issues were the control of early somatic effects of radiation exposure and their impact on mission safety. Few astronauts, if any, were expected to make more than one high-profile trip to the Moon so that career exposures were of secondary importance. In this context, the galactic cosmic ray (GCR) background exposures at rates of 150 to 200 mGy/yr were not of great concern (refs. 1 and 2).

With the advent of the Space Shuttle, the context of an astronaut changed from space explorer to space worker and career exposure limits came into focus with late somatic effects seen as the ultimate limiting factor on mission activity (ref. 3). Such a radical shift in astronaut exposure patterns led to a reevaluation of the importance of low-level GCR background exposures. (A detailed review is given in ref. 2.)

Within a few years of the discovery of particles of high charge and energy (HZE) as components of the GCR, the unique pattern of energy deposit on the microscopic scale raised issues with respect to effects on living cells (ref. 4). Also, the light flashes induced by proton reactions and HZE ion passage through the vitreous humor observed by astronauts in space had already been predicted in the infancy of the space program (ref. 5). Although radiobiological knowledge has greatly improved, our ability to estimate risk to the astronaut from such exposures is still quite uncertain (ref. 6). Even a crude estimate using the linear energy transfer (LET) dependent quality factor (ref. 2) results in as much as 1.2 Sv/yr exposures, depending on shielding near solar minimum. This shows a large potential impact on the career of a space worker or a deep-space explorer.

Clearly, 1.2 Sv/yr is an important number, but one must hesitate in applying it to astronaut risk because it implies extrapolation from the human database for late somatic effects that are based primarily on X-ray and γ-ray exposures (refs. 7 and 8). Evidence is growing of biological end points which are peculiar to high-LET HZE exposures that are not produced by X-rays or γ-rays for which the relative biological effectiveness (RBE) is infinite or undefined. Evidence that the usual extrapolation of risk from the γ-ray database is inadequate has been provided by the measurement of sister chromatid exchanges in resting human lymphocytes irradiated with ^{238}Pu α-particles (ref. 9), by the observation of abnormalities in stem cell colonies surviving similar α-particle irradiation (ref. 10), and by the partial disintegration of chromosomes after irradiation with high-energy heavy ion beams to simulate space radiation (ref. 11). In these examples, a quality factor related to RBE becomes meaningless because at doses comparable to that delivered by one particle (or a few particles), and for radiation effects that are not manifest for low-LET radiation (e.g., X-rays), the RBE becomes infinite. Thus, new methods to predict the

risk resulting from exposure to GCR radiation must be developed.

The biological response of living tissues depends (in part) on the temporal and spatial fluctuations of the energy deposits within the tissue system. Such fluctuations depend not only on the specific environment to which the astronaut is exposed but also on how that environment is modified by interaction with the astronaut's body in reaching the specific tissues. Only by knowledge of the specific radiation types and their physical properties at the tissue site can a basis for estimating astronaut risk be found. Even if the environment to which the astronaut is exposed is known precisely, the energy deposit within specific tissues deep in the astronaut's body are, for the most part, known only through theoretical estimates and are, therefore, limited by the uncertainty in the calculational models. Clearly, an accurate conversion of the astronaut's environment to estimates of exposure fields at specific tissue sites is a high priority in the space-radiation protection problem.

Apart from the issues of the astronaut's self-shielding factors and uncertainty in human response to the HZE particles, radiation shielding implies some control over the radiation environment to which the astronaut is exposed. The traditional structural material within the space program has been aluminum. The absorbed dose at solar minimum from an annual GCR exposure behind an aluminum shield is shown in sketch A. The absorbed dose increases to a maximum at 3 to 4 g/cm^2 and declines to the free-space value at about 30 g/cm^2. Clearly, no shielding advantage is found in reducing the energy absorbed by the astronaut, and if any protection is provided, it results from changes in the microscopic pattern of the energy-absorption events (ref. 12).

Herein, we examine the modification of the physical parameters of the attenuated GCR environment in various materials to develop an understanding of the qualitative changes in environmental components as a function of shield composition (including tissue-equivalent shields). In this context, one begins to appreciate the role of nuclear cross sections in modifying the local environment and the associated microscopic fluctuation in the energy-absorption events. Furthermore, we will begin to understand the effects of nuclear cross-section uncertainty as it applies to the change in the microscopic energy-absorption fluctuations. We shall assess the importance of these local environmental modifications on biological systems in terms of conventional dosimetry by using defined quality factors and a biological model that is dependent on track structure.

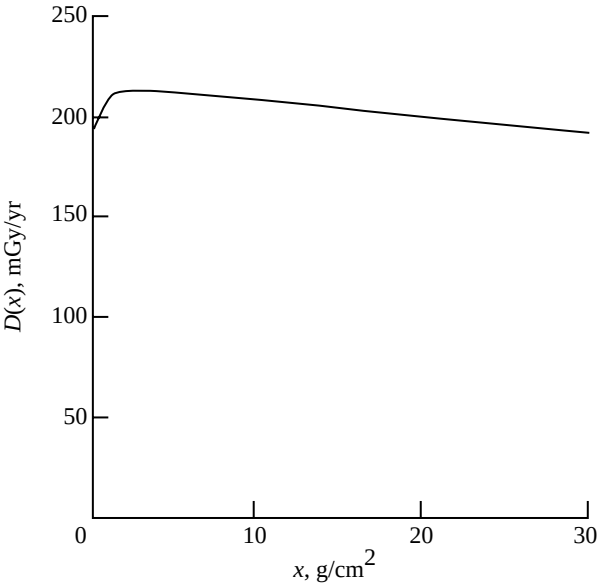

Sketch A

Although the human risk associated with such exposure is uncertain, radiobiology experiments with immortal cell populations (cell cultures that can be sustained indefinitely) have yielded biological data suitable for estimating GCR exposure effects on those specific cell populations. The response of the C3H10T1/2 mouse cell cultures (ref. 13) has been used to evaluate shield properties for the biological end points of clonogenic death and neoplastic transformation (ref. 12). Clonogenic death is closely associated with the early response of radiation sickness (nausea, vomiting, erythema, etc.), and neoplastic transformation is related to cancer induction. A cell-repair kinetics model including track-structure effects for the C3H10T1/2 system (refs. 13–15) provides a basis for studying shield performance.

In the present paper, we first discuss the problem of radiation risk assessment in the context of microdosimetry. We then examine the shield parameters related to shield performance and evaluate the performance on the basis of conventional risk assessment and the C3H10T1/2 cell model. On this basis we examine the effects of shield-material selection on shield design. Light hydrogenous compounds are shown to hold great promise as high-performance shield materials. Encouraged by this prospect, we then examine the effects of hydrogen-bearing compounds as potential space structural components. A pilot experiment to study such effects is described.

The importance of hydrogenous materials in modifying the biologically important components of ion beams makes these studies important in evaluating

the therapeutic value of heavy ion beams in medical applications. Indeed, the computational procedures used, the quality of the nuclear database, and the biological response models should be useful in the design of therapeutic procedures.

Microscopic Fluctuations and Biological Response Models

The response of living tissue (refs. 3 and 8) to a dose D_γ with low LET is represented by a sensitivity coefficient k_γ and a quadratic coefficient D_o as

$$R_\gamma = k_\gamma D_\gamma \left(1 + \frac{D_\gamma}{D_o}\right) \tag{1}$$

where R_γ is either the risk of inducing a specific end point or the level of severity. The parameter D_o is dose-rate dependent and is on the order of 1.2 Gy for dose rates larger than 50 mGy/day (refs. 3 and 8). We assume a low dose rate herein so that D_γ^2 may be neglected, where

$$R_\gamma = k_\gamma D_\gamma \tag{2}$$

The concept of dose as a physical or chemical insult per unit mass of tissue is a carryover from the concepts of pharmacology and assumes that dose is a measure of effects on individual cells (ref. 16). Tissue cells are, in fact, not all equal at low exposures because the energy deposits are quantized and energy is deposited in only a fraction of cells; similarly, volumes within a given cell are not all equally sensitive. In general, the absorbed dose D is not a good measure of biological damage because this average quantity can be decomposed (ref. 16) as follows:

$$D = \frac{\sum \epsilon_i}{V N_E} = \frac{\sum \epsilon_i}{V N_H} \frac{N_H}{N_E} \tag{3}$$

where V is the sensitive site volume (unit density), ϵ_i is the energy absorbed per site hit (referred to as the "hit size" of the ith event), and N_E is the number of exposed sites. At a low dose, not all sites are hit, and so the number of site hits N_H is less than the number of sites exposed. Only when $N_H \to N_E$ is D meaningful in terms of individual cell response (ref. 16). The fraction of sites that are hit at low exposure (that is, $N_H \ll N_E$) is

$$\frac{N_H}{N_E} \approx \sigma_g \phi \tag{4}$$

where σ_g is the site geometric cross section and ϕ is the charged-particle fluence within the tissue system. In reality, the cross section can be larger than the geometric cross section because of the δ-ray diffusion for which the number of site hits is increased by sites hit far from the ionizing particles path. The fluence ϕ is related to the macroscopic absorbed dose D and to the value of the unrestricted LET (L) as

$$\phi = 6.24 \frac{D}{L} \tag{5}$$

where ϕ is given in particles/μm^2, D in Gy, and L in keV/μm. For γ-rays, L_γ corresponds to the secondary electrons generated and has a value of about 0.25 keV/μm; the corresponding ϕ_γ is an effective secondary electron fluence that is dependent on the photoabsorption coefficient and the γ-ray fluence.

The average hit size ($\bar{\epsilon}$) is given as

$$\bar{\epsilon} = \sum_i \frac{\epsilon_i}{N_H} \tag{6}$$

and is known from basic physical principles and specifications of the site volume V. The mean number of hits per exposed site is then

$$\frac{N_H}{N_E} = \frac{DV}{\bar{\epsilon}} \tag{7}$$

and is related to the number of hit sites assuming Poisson statistics. We have estimated $\bar{\epsilon}$ from the theory of Xapsos et al. (ref. 17) for various ion types as shown in figure 1(a) for a 1-Gy exposure and 0.1-μm site size corresponding approximately to the width of a single chromatin strand and its immediate environment. In figure 1 we have ignored contributions from fragmenting nuclei of the biological target. The effect of site size is shown by comparing the 0.1-μm site size with the 0.5-μm site size in figure 1(b). Note that the hit size and average number of hits increase with the site size. The recently defined quality factors (ref. 7) are also shown in figure 1(c). The region of unit quality factor for this 1-Gy exposure is marked by a sizable fraction of hit sites with a fraction of keV hit size, and the corresponding excess fatal cancer risk to this exposure would be about 3 percent. In distinction, the 100-keV/μm exposure has a quality factor near 20 to 30 and would result in an estimated excess cancer risk of 60 to 90 percent. The mean hit size in this case is several tens of keV, and a small fraction (less than 1 percent) of the sites are, in fact, hit. The HZE particles show a smaller hit size because of their range and δ-ray diffusion than the smaller ions at the same LET. A corresponding increase occurs in the number of sites hit. A further distinction of HZE exposure is

that a clustered group of contiguous cells (or sites) is affected by a single ion passage because of their range and δ-ray diffusion (ref. 18) in distinction to smaller ions of the same LET.

Figure 1 aptly illustrates the great variability of the microscopic fluctuations expressed previously as the mean hit size and the fraction of sites hit for various radiation field components. Although the meaning of this variability is somewhat represented by the quality factor, as noted in figure 1, an added distinctive feature of the HZE exposures is that large clusters of contiguous cells are affected. We do not yet understand the radiation response of many of the GCR components, but it is surely the changes wrought by shield materials on these microscopic fluctuations that will serve as the primary means of radiation protection and not a decline in the energy absorbed with the addition of shield material. (See sketch A.)

Conventional Risk Assessment

According to equation (1), excess cancer risks for humans are estimated based on coefficients derived from X-ray and γ-ray exposures. The conventional method of extrapolating the human database to high-LET exposures is to replace D_γ in equation (1) by the dose equivalent H given by

$$H = QD \tag{8}$$

where Q is the LET-dependent quality factor shown in figure 1(c). Equation (8) follows from analogy with the relative biological effectiveness given for γ-ray and ion exposure levels D_γ and D_i which result in the same biological end point by

$$\mathrm{RBE} = \frac{D_\gamma}{D_i} \tag{9}$$

We note that the quality factor is a defined quantity (not given by a measurement) and represents trends of measured RBE in cell culture, plant, and animal experiments. The RBE values depend on end point, dose, dose rate, and quality of the radiation usually represented by LET. Usually, RBE is assumed to reach a maximum value (denoted by $(\mathrm{RBE})_M$) at sufficiently low dose as related to the initial slopes of the response curves of each radiation type (refs. 3 and 19). Furthermore, the dose at which $(\mathrm{RBE})_M$ is achieved is assumed to be dose-rate dependent as shown in figure 2. The values of RBE from which Q is defined as a function of LET are largely for high dose rates at the 0.1-Gy level of exposure for which fission neutrons have $\overline{Q} = 25$ corresponding to a γ-ray exposure of 2.5 Gy. The RBE values for lower levels of exposure and/or lower dose rate are much larger (ref. 19), as shown in table 1, and occur for lower exposure and dose rates than were used in deriving Q. In that the achieving of $(\mathrm{RBE})_M$ is accelerated at a low dose rate, the RBE values in table 1 may, in fact, be more appropriate for space exposures. This is one source of the rather large uncertainties in space-radiation exposure risks. The second source of uncertainty concerns the response to HZE exposures for which little is known. The assumption is made that single-ion track effects for which γ-ray exposures have no analog are possible. One such mechanism was suggested by Todd (ref. 18) in which the cells exposed at 0.25 Gy have a high probability of being transformed whereas the dead cells of the track core must be replaced, thus causing promotion to a cancer growth by this one event. (See fig. 3.) The RBE for such results is undefined (infinite), and extrapolation from the human database is not possible.

Table 1. $(\mathrm{RBE})_M$ for Fission Neutrons

Tumor induction (approximate)	3–200
Life shortening	15–45
Transformation	35–70
Cytogenic studies	40–50
Genetic end points in mammalian systems	10–45
Other end points:	
Lens opacification	25–200
Micronucleus assay	6–60
Testes weight loss	5–20

The use of an LET-dependent quality factor as related to dose equivalent implies additivity of diverse components in estimating risk. Such assumptions may underestimate the actual risk as was discussed by Scott (ref. 20). Furthermore, risks associated with different time intervals are likewise not additive, especially if radiation proves to be an effective promotion factor in carcinogenic response (ref. 21). For low-LET exposures, substantial repair is often operative and results in reduced risk. For high-LET exposures, dose-rate enhancement effects are possible in which risk is substantially increased at lower dose rates (ref. 22) as shown in figure 4.

The uncertainties in radiation-induced risk have been estimated in the NASA Radiation Health Program (ref. 6) and are presented in figure 5. In the approximation used here, the risk is assumed to be related to the total value of dose equivalent. This assumes that the dose-response curve is of similar shape for each radiation component which is linear at low

dose and dose rate. The excess risk (the added risk due to exposure) is then given by

$$R = k_\gamma H = k_\gamma (H_x + H_z) \tag{10}$$

where H is the dose equivalent (given in Sv), H_x is the component of dose equivalent due to low-LET radiation, and H_z is the dose equivalent due to the HZE component of the radiation. By making the further approximation that the uncertainties in k_γ and H_x are negligible in comparison with the uncertainty in H_z, we obtain

$$\Delta R = k_\gamma \frac{\Delta H_z}{H_z} H_z \equiv k_\gamma U H_z \tag{11}$$

so that the net effect of the uncertainty in R is to increase the relative risk, which becomes

$$R + \Delta R = k_\gamma H + k_\gamma U H_z = k_\gamma H_u \tag{12}$$

This equation defines an effective dose equivalent (H_u) which corresponds to the increased risk due to uncertainties. If a limit $\mathcal{L}$ is defined on the basis of excess risk R, then it is required that

$$R + \Delta R \leq \mathcal{L} \tag{13}$$

where $\mathcal{L}$ is the defined limit of acceptable risk. A safety factor (S) can be defined with reference to equation (12). Let S be an upper bound on the estimated value of the uncertainty in HZE dose equivalent (that is, $S = nU$), where $n = 1, 2 \ldots$ corresponds to the number of standard deviations required to establish an acceptable safety margin. Then, equation (12) becomes

$$R + \Delta R = k_\gamma H + k_\gamma S H_z = k_\gamma H_s \tag{14}$$

where the effective dose equivalent, including the safety factor, is given by

$$H_s = H + S H_z$$

Alternatively, the HZE component in equation (10) can be increased according to

$$H_z' = H_z + S H_z = (1 + S) H_z$$

This formulation suggests the possibility of using the ratio between experimental values of RBE (as appropriate for GCR exposure) and $\overline{Q}$ as an approximation for $1 + S$; for example, the measured RBE for life shortening in mice has been reported to be as large as 80 for fission neutrons (ref. 22), whereas the estimated value of $\overline{Q}$ is on the order of 20. Thus, an estimate for the value of S would be 3 (which corresponds to an effective dose equivalent that is 300 percent greater for HZE exposure than would be obtained from currently accepted conventional dosimetric analyses). Such a value (300 percent) might be considered reasonable from a radiobiological point of view and may not be too restrictive on mission design and operations (ref. 23).

In the present study we will ignore the uncertainty in risk estimates ($S \equiv 0$) and apply the quality factor $\overline{Q}$ in estimating the dose equivalent that is assumed to be linearly related to risk. The variation of dose equivalent with shield thickness and composition will be one means of estimating shield effectiveness.

Track-Structure Repair Model

Although the use of quality factors may give some indication of the attenuation of biologically important components, their use in space protection against HZE particles has specifically not been recommended (ref. 3), and we consider herein a test biological system for the study of shield properties. Ionizing radiation interacts with matter through the formation and interaction of radicals which we call the nascent lesions. These highly active chemical species may result in structural change or restore the cell to its initial state, but they are finally consumed. If these structural changes occur within the DNA and cannot be repaired by enzymatic processes, then subsequent generations may exhibit new characteristics or the cell may be unable to undergo cell division for which clonogenic death occurs.

Many ways exist in which the DNA can be changed to cause cell death, but only a few specific changes are allowed to reach other biological end points. First, we treat those lesions that lead to cell death and write kinetic equations (ref. 13) for the time development of the cell population $n_i(t)$ with i-fold lesions as

$$\dot{n}_0 = \sum_{i=1}^{\infty} \alpha_{r_i} n_i - k n_0 \tag{15}$$

$$\dot{n}_i = \sum_{j=0}^{i-1} k_{i-j} n_j - k n_i - \alpha_i n_i \tag{16}$$

$$\dot{n}_d = \sum_{i=1}^{\infty} \alpha_{m_i} n_i \tag{17}$$

where k_i is proportional to the charged-particle flux (primary and secondary), α_{r_i} is the repair rate,

α_{m_i} is the misrepair rate, and n_d is the population of misrepaired cells. Conservation of cells within a given cell cycle requires that $k = k_1 + k_2 + \ldots$ and $\alpha_i = \alpha_{r_i} + \alpha_{m_i}$. The ratio $\alpha_{r_i}\alpha_i^{-1}$ is the kinetic repair efficiency and m_d is the smallest i for which the repair efficiency is zero.

The k_i kinetic coefficients are related to the Katz model (ref. 24) for the highly repair efficient, stationary G_1 phase cells as

$$k_1 = (m_d!)^{1/m_d}\frac{\dot{D}_\gamma}{D_0} \tag{18}$$

$$k_{m_d} = \sigma\phi \tag{19}$$

where all other values of k_i are taken as zero (refs. 25 and 26) and the remaining quantities are all given by Katz as

$$\dot{D}_\gamma = \left(1 - \frac{\sigma}{\sigma_0}\right)L\phi \tag{20}$$

in which ϕ is the local charged particle flux (primary and secondary), L is their corresponding LET, and σ is approximated by using the Katz model. (See ref. 13.)

The cellular track model of Katz et al. (ref. 24) attributes biological damage from energetic ions to the secondary electrons (δ-rays) produced along the path of the ion. The effects caused by energetic ions are correlated with those of γ-rays by assuming that the response in sensitive sites near the path of the ion is part of a larger system irradiated with γ-rays at the same dose. The response due to ion effects is then approximately related to the γ-ray response and the δ-ray dose surrounding the path of the ion. For a multitarget response with target number m, the inactivation of cells by γ-rays is assumed to follow a Poisson distribution reflecting the random accumulation of sublethal damage, with a radiosensitivity parameter D_0.

For the inactivation of cells by ions, two modes are identified: "ion-kill" which corresponds to intratrack effects and "gamma-kill" which corresponds to intertrack effects. Here, the ion-kill mode is unique to ions corresponding to single-particle inactivation of cells described by the cross section σ. The inactivation cross section for a sensitive site whose response to radiation is ahistoric is determined as

$$\sigma = \int_0^\infty 2\pi t\, dt\left(1 - e^{-\overline{D}/D_0}\right)^m \tag{21}$$

where $\overline{D}$ is the average dose at the sensitive site from the δ-rays of the ion. The evaluation of the cross section is separated by Katz et al. (ref. 24) into a so-called grain-count regime (where inactivation occurs randomly along the path of the particle) and into the so-called track-width regime (where many inactivations occur and are said to be distributed like a "hairy-rope"). In the grain-count regime, σ may be parameterized as

$$\sigma = \sigma_0\left(1 - e^{-Z^{*2}/\kappa\beta^2}\right)^m \tag{22}$$

where σ_0 is the saturation value of the cross section, the effective charge number is given by

$$Z^* = Z\left(1 - e^{-125\beta/Z^{2/3}}\right) \tag{23}$$

and κ is a parameter related to the radius of the sensitive site (a_0) by

$$\frac{D_0 a_0^2}{\kappa} \approx 2 \times 10^{-7}\text{erg/cm} \tag{24}$$

The transition from the grain-count regime to the track-width regime is observed to take place at a value of $Z^{*2}/\kappa\beta^2$ of about 4; we are in the grain-count regime at lower values and in the track-width regime at higher values.

The fraction of the cells damaged in the ion-kill mode is $P = \sigma/\sigma_0$; note that in the track-width regime, $\sigma > \sigma_0$, and the assumption is made that $P = 1$. The track model assumes that a fraction of the dose of the ion $(1 - P)$ acts cumulatively with that for other particles to inactivate cells in the gamma-kill mode.

The repair coefficients are found to be cell-phase dependent, and the G_1-phase repair efficiencies are near maximum for $i < m_d$ and near zero otherwise. The exponential population showed relatively high single-lesion repair efficiency and much lower multiple-lesion repair efficiencies (see table 2) in analyzing the repair-dependent experiments of Yang et al. (ref. 15). As examples, the G_1 repair-enhanced exposures (made by delayed plating, the process by which G_1 exposed cells are delayed in the G_1 phase for 24 hours after exposure) and exponential phase repair exposures (made by immediate plating, the process whereby G_1 exposed cells are separated and immediately introduced to nutrients after exposure) are compared with the present results in figure 6 for various ions (ref. 14) and with fractionated exposures from 225-kVp X-rays (ref. 15) in sketch B. We will use this model to study the functional dependence of RBE at low total dose and low dose rate for G_1 phase and exponential phase repair processes.

Table 2. Parameters for Track-Structure Repair Model

(a) Survival repair rates and repair efficiencies

Rate and efficiency	G_1 phase for—		Exponential phase for—		
	$i=1$	$i=2$	$i=1$	$i=2$	$\geq m_d$
α_i (rate), per hr	0.25	0.125	0.25	0.125	<0.08
$\alpha_{r_i}\alpha_i^{-1}$ (efficiency)	>0.97	>0.84	0.7	0.118	≈0

(b) Katz C3H10T1/2 cell parameters

Biological response	σ_0, cm^2	k	m_d	D_0, Gy
Survival	5×10^{-7}	750	3	2.8
Transformation	7×10^{-11}	475	3	150

(c) Transformation repair rates and repair efficiencies

Rate and efficiency	G_1 phase for—		Exponential phase for—		
	$i=1$	$i=2$	$i=1$	$i=2$	$\geq m_d$
α_i (rate), per hr	0.25	0.125	0.25	0.125	≤0.08
$\alpha_{r_i}\alpha_i^{-1}$ (efficiency)	1.0	1.0	0.99	0.70	0

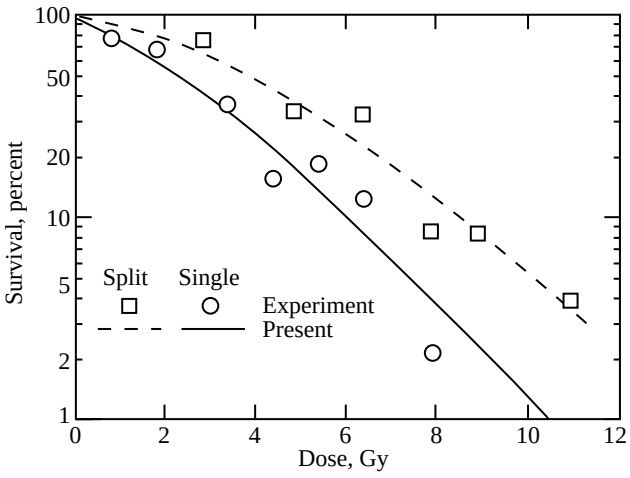

Sketch B

We consider now a special solution of equations (15) to (17) for an exposure field with a low constant dose rate ($\alpha_i \gg k_j$ for all i,j). At low dose rates the populations of cells with lesions can be approximated as

$$n_1(t) \approx \frac{k_1\, n_0(t)}{\alpha_1} \tag{25}$$

$$n_2(t) \approx \frac{k_1^2\, n_0(t)}{\alpha_1 \alpha_2} \tag{26}$$

$$n_3(t) \approx \left(\frac{k_1^3}{\alpha_1 \alpha_2 \alpha_3} + \frac{k_3}{\alpha_3} \right) n_0(t) \tag{27}$$

In the case of low total exposure, $n_0(t)$ may be taken as constant and the accumulation of misrepaired cells is written as

$$\begin{aligned} \frac{n_m(t)}{n_0} \approx{}& \frac{\alpha_{m_1}}{\alpha_1}\, 6^{1/3} \frac{(1-P)D}{D_0} \\ &+ \frac{\alpha_{m_2}}{\alpha_2}\, 6^{2/3} \frac{(1-P)^2 \dot{D} D}{D_0^2 \alpha_1} \\ &+ \frac{\alpha_{m_3}}{\alpha_3}\, 6\, \frac{(1-P)^3 \dot{D}^2 D}{D_0^3 \alpha_1 \alpha_2} + \frac{\alpha_{m_3}}{\alpha_3} \frac{\sigma}{L} D \end{aligned} \tag{28}$$

where $\dot{D}$ is the dose rate and $P = \sigma/\sigma_0$. In the case of an exponential population, $\alpha_{m_1}/\alpha_1 \approx 0.3$ so that the first term is always dominant over the second and third terms for very low dose-rate exposures ($\dot{D}\alpha_i^{-1} \ll D_0$). The $(\mathrm{RBE})_M$ is found to be

$$(\mathrm{RBE})_M = 1 - P + 6^{-1/3} \frac{\alpha_{m_3}}{\alpha_3} \frac{\alpha_1}{\alpha_{m_1}} \frac{\sigma}{L} D_0 \tag{29}$$

as was found for our earlier result (ref. 25). If the repair efficiency of the G_1 phase is high

$(\alpha_{m_1}/\alpha_1 \ll \dot{D}/\alpha_i D_0)$, then the higher order terms of equation (28) cannot be ignored in determining the RBE for which important dose-rate-dependent factors exist whenever $\dot{D} \gg \alpha_i D_0 \approx 0.01$ Gy/min. At much lower dose rates ($\dot{D} \ll 0.01\alpha_{m_1}/\alpha_1$ Gy/min), the $(\mathrm{RBE})_M$ given by equation (29) is obtained. A parameter study using the data in figure 6 shows that $\alpha_{m_1}/\alpha_1 < 0.03$, which corresponds to a 97-percent repair efficiency as noted in table 2.

In exposures by galactic cosmic rays, the dose rate is very small:

$$\dot{D} \approx 0.5m \text{ Gy/min} \ll \alpha_i D_0 \approx 10m \text{ Gy/min} \quad (30)$$

for which the nonsurviving fraction is

$$\frac{n_m(t)}{n_0} \approx \frac{\alpha_{m_1}}{\alpha_1} 6^{1/3} \frac{(1-P)D}{D_0} + \frac{\alpha_{m_3}}{\alpha_3} \frac{\sigma}{L} D \quad (31)$$

One may similarly show that the fraction of transformed cells is given by the same functional form as $n_m(t)/n_0$, with the kinetic parameters associated with transformation as given in table 2.

Galactic Cosmic Ray Transport

To predict the propagation and interactions of the deep-space nucleons and heavy ions through various media, the galactic cosmic ray (GCR) transport code, HZETRN (ref. 27), that was developed at the Langley Research Center is used. This code includes the transport of high-energy heavy ions up to an atomic number (Z) of 28 and solves the fundamental Boltzmann transport equation. With the straight-ahead approximation and the target secondary fragments neglected, the transport equation is written as

$$\left[\frac{\partial}{\partial x} - \frac{\partial}{\partial E}\widetilde{S}_j(E) + \sigma_j(E)\right]\phi_j(x,E) = \sum_{k \geq j} \int_E^\infty \sigma_{jk}(E,E')\,\phi_k(x,E')\,dE' \quad (32)$$

where

$\phi_j(x,E)$	flux of ions of type j with atomic mass A_j having energy E (in units of MeV/amu) at spatial location x
σ_j	macroscopic total nuclear-absorption cross sections
$\widetilde{S}_j$	change in E per unit distance
σ_{jk}	differential nuclear-interaction cross sections

To evaluate the flux of particles of type j with energy E, the input database required consists of the stopping power, the macroscopic total nuclear cross sections, and the differential nuclear-interaction cross sections. The differential cross sections σ_{jk} describe the production of type j particles with energy E by type k particles of energies $E' > E$. These data are those compiled for the present HZETRN code system (refs. 2 and 27).

The absorbed dose D due to energy deposition at given location x by all particles is calculated according to

$$D(x) = \sum_j \int_0^\infty S_j(E)\,\phi_j(x,E)\,dE \quad (33)$$

For human exposure, the dose equivalent is defined by the quality factor Q which relates the biological damage incurred because of any ionizing radiation to the damage produced by soft X-rays. In general, Q is a function of linear energy transfer which depends on both particle type and energy. For dose-equivalent calculations, the quality factors used are those defined by the International Commission on Radiological Protection in 1990 (ref. 7). The values of dose equivalent H are computed as

$$H(x) = \sum_j \int_0^\infty Q_j(E)\,S_j(E)\,\phi_j(x,E)\,dE \quad (34)$$

In addition to the standard dosimetric techniques used to evaluate health risks due to high-energy, low-dose-rate exposure from the GCR heavy ions, the fractions of cell destruction and transformation are calculated by using radiosensitivity parameters derived from biological experiments (ref. 13). The nonsurviving fraction is found by using

$$\frac{n_m(t)}{n_0} = \sum_j \int_0^\infty \left\{6^{1/3}\,\frac{\alpha_{m_1}}{\alpha_1}\frac{[1-P_j(E)]\;S_j(E)}{D_0} + \sigma(E)\right\}\phi_j(x,E)\,dE \quad (35)$$

where $\sigma(E)$ is the appropriate Katz cross section for ion j. A similar expression applies for the evaluation of the fraction of transformed cells. The cellular parameters used in the present analyses are given in table 2.

Characteristics of Shield Materials

Shielding the work area of an astronaut crew will always result in a wall thickness (given in cm) that is small in comparison with the linear dimension of the crew compartment. The shield mass is then proportional to the areal density (given in g/cm^2) which we use as the appropriate measure of shield thickness.

The shield properties depend on the basic atomic/molecular and nuclear cross sections. Atomic/molecular stopping cross sections depend on the number of electrons per unit volume, the electronic mean excitation energy, and tight binding corrections for the inner shell electrons. The stopping range in units of areal density are shown in figure 7 for several ions and greatly differing materials. Materials with the most electrons per unit mass, the least mean excitation energy, and the least tight binding corrections make the best energy absorbers. Thus, liquid hydrogen is a favored material and lead is less efficient as an energy absorber.

The nuclear cross sections relate not only to the free paths for nuclear reaction but to the nature of the reaction products. The projected nuclear cross section per unit mass of material is the appropriate parameter as shown in figure 8. Equally important is the nature of the reaction products produced. The production cross sections per unit mass of shield at high energy are shown in figure 9. Although the low Z shields are favored by the short free paths of figure 8, the effects of the products produced in figure 9 are unclear.

The microscopic fluctuations in the energy-absorption events of several ions are represented parametrically as a function of LET in figure 1. Although LET is a less-than-perfect indicator of the microscopic patterns, it is a useful physical quantity to indicate radiation quality; it remains the focus of many biological investigations and serves as the basis of conventional radiation protection practice (ref. 7). The transmitted differential LET spectra through four shield materials are shown in figure 10. The left-hand discontinuities are associated with the minimum ionization at relativistic energies for each ion type. The far-left discontinuity consists of hydrogen isotopes followed by helium isotopes and so on through Ni isotopes. The smaller right-hand discontinuities are associated with maximum ionization in the stopping region. At one time these stopping ions were suspected of being the primary hazard (ref. 4). One should keep in mind that an uncertainty factor of 2 to 3 exists for the LET region above 100 keV/μm because of an uncertainty in the nuclear cross sections (ref. 28). Even adding energy dependence in the nuclear cross sections resulted in a 50-percent increase above 100 keV/μm (refs. 29 and 30).

In each case, we see the attenuation of the highest LET components in each material with liquid hydrogen being the most efficient and lead the least efficient. When viewing the transmission curves for aluminum (fig. 10(c)), one notes that the spectral changes are minimum in the range of several keV/μm and that the LET spectrum attenuates at higher LET and amplifies at lower LET. This pivotal LET value, which is a function of the shield composition, increases to 40 to 50 keV/μm for lead and decreases to less than 1 keV/μm for liquid hydrogen. The pivotal LET value is associated with the loss of a given species because of attenuation being matched by the production of that same species in nuclear events. The location of the pivotal LET value is critical to the changes in the microscopic fluctuations in energy-absorption events which ultimately affect the biological response. Clearly, the shield effectiveness is intimately related to the nature of the nuclear cross sections through the change in the microscopic fluctuations in biological exposure, but selection of the shield material must wait for improved knowledge of the biological response.

Illustrations of Shield Effectiveness

We examine the aforementioned concepts in terms of two biological models. The first model is the conventional risk-assessment method (ref. 7) using the quality factor as a function of LET. The second model is a track-structure-repair kinetic model (ref. 13) for the C3H10T1/2 mouse cell for which a large body of experimental data exist with various ions in which repair kinetic studies have been made (refs. 14 and 15). We will evaluate the effectiveness of these materials to reduce the biological effects as a function of shield mass.

The distribution of particle fluence at 5 g/cm^2 is converted (ref. 30) to the distribution of an absorbed dose over the same LET intervals in figure 11. Also in figure 11 is the dose-equivalent distribution obtained by multiplying the absorbed dose at each LET by the corresponding quality factor as shown in figure 1(c). A large contribution to the dose equivalent results from ions in the LET interval ranging from 10 to 10^3 keV/μm. Shown in figure 12 are the geometric hit frequency, the initial level of cell injury, and the unrepaired cell injury leading to clonogenic death in a C3H10T1/2 mouse cell population as calculated in reference 13.

The attenuation of dose equivalent as a function of areal density is shown in figure 13(a). The

modification of the LET distribution as it depends on shield composition is obviously a critical issue. Lead shielding with the LET pivot point near the peak of the LET contributions to dose equivalent is a poor shield material for the GCR environment. Clearly, the lowering of the LET pivot point enhances the shield performance of the materials, with liquid hydrogen being an optimum selection. Liquid hydrogen, is of course, a difficult material to use because it is a liquid with a very low temperature. Evaluation of the relative gain made by the use of off-optimum shield materials that are more useful in construction is a critical issue. Furthermore, the adequacy of results derived by using quality factors to represent biological systems is still questionable for HZE particles.

A second illustration is found using a model for neoplastic transformation of the C3H10T1/2 mouse cell for which sufficient experimental data exist for developing a reasonable model (ref. 13). The repair kinetics model was solved at a low dose rate for a 1-year exposure behind the shields in figure 10. Figure 12 shows that although the cell is most often hit by protons and helium ions, the probability of injury is small and the repair efficiency is high with little permanent injury. Conversely, a high probability of injury and near-zero efficiency of repair occur from hits of silicon and iron ions. As a consequence, most clonogenic death from GCR exposure comes from ions with an LET above 10 keV/μm (ions above relativistic carbon). Radiation injury from these ions shows minimal cellular repair. As a result, dose protraction (an extended exposure period at the same accumulated dose) for GCR exposure will be less effective in reducing the biological response.

The change in radiation-induced transformations for a 1-year exposure in space is shown in figure 13(b). Although the attenuation characteristics for various shield materials are qualitatively similar to the attenuation of dose equivalent shown in figure 13(a), important quantitative differences exist. This is best seen in terms of the attenuation of the transformation rate in a given material compared with the attenuation of the dose equivalent in the same material. The relative attenuation for the transformation rate and dose equivalent are shown in figure 14 for the data shown in figure 13.

The rates of attenuation of biological effects as estimated by the two risk models are similar only for the liquid hydrogen shield. This implies that the quality factor in ICRP-60 (ref. 7) represents in some way the dependence on radiation quality in this case. The quality factor is less useful for shields containing nonhydrogenous components and is a poor indicator for lead shields. Very similar results are found as well for clonogenic death of the C3H10T1/2 cells (ref. 13). What is very clear from figure 14 is that the use of local materials (such as regolith) for a lunar base or for martian exploration shielding designs based on quality factors remains in great doubt. A meaningful design can be made only when improved risk models and the nuclear fragmentation parameters become available.

Proposed Shield-Performance Index

In an attempt to assign a quantitative measure of shield performance, we consider a track-structure kinetics model of the C3H10T1/2 cell system for clonogenic death and transformation (ref. 12). Results of this model for a 1-year exposure behind a 5 g/cm^2 aluminum shield is shown in figure 12. We have further evaluated this model for various shield materials used in the present study at the various depths in figure 13(b). We note that the depths in units of areal density are proportional to the total shield mass of a large shielded region. The exposure conditions assume a stationary G_1 phase exposure for a constant dose rate over the 1-year period. We compare the cell transformation behind an aluminum shield ($T_{\mathrm{Al}}(x)$) of areal density x with the cell transformation for a different material ($T_m(x)$) of the same areal density. Thus,

$$\text{Cell-transformation ratio} = \frac{T_{\mathrm{Al}}(x)}{T_m(x)} \qquad (36)$$

as a measure of relative biological protection of the two materials.

As shown previously, the cell-transformation ratio does not correlate well with the dose equivalent. (See ref. 12 and fig. 14 herein.) The separation of physical and biological factors is accomplished by using basic concepts in microdosimetry. The physical factors are the moments of the LET distribution and are determined by the shield properties (ref. 12). A new quantity that correlates well with cell transformation behind various shield thicknesses and materials is defined from the postulate of Bond, Varma, and Sondhaus (ref. 16). The risk function within a cell population for the radiation of the LET (L) value is approximated as

$$R_L = 6.24\ \sigma_g \frac{D_L}{L} \sum B_i \left\langle \epsilon^i \right\rangle \qquad (37)$$

Because average lineal energy is numerically equal to the LET (that is, $\langle \epsilon^n \rangle \propto \langle L^n \rangle$) in a mixed

Table 3. Moments of LET Behind Various Shield Materials for a 1-Year Exposure of GCR at Solar Minimum and Their Correlated Quantities

Shield		Moments of LET, $(\mathrm{MeV/cm})^i\mathrm{cm}^{-2}$, for—						
Material	Thickness, $\mathrm{g/cm}^2$	$i=0$	$i=1$	$i=2$	$i=3$	$i=4$	$p_m(x)$	$P_m(x)$
Free space		1.29×10^{8}	1.00×10^{9}	1.70×10^{12}	3.70×10^{16}	118×10^{19}		
Al	2	1.32×10^{8}	0.916×10^{9}	0.47×10^{12}	0.278×10^{16}	4.84×10^{19}	10.6×10^{15}	1
	5	1.35	.897	.365	.201	3.42	8.78	1
	10	1.38	.866	.253	.124	2.05	6.57	1
Fe	2	1.34×10^{8}	0.938×10^{9}	0.493×10^{12}	0.303×10^{16}	5.41×10^{19}	12×10^{15}	0.88
	5	1.35	.942	.407	.235	4.14	10.4	.85
	10	1.38	.923	.302	.158	2.72	8.11	.81
Polyethylene	2	1.31×10^{8}	0.849×10^{9}	0.4×10^{12}	0.22×10^{16}	3.65×10^{19}	8.33×10^{15}	1.27
	5	1.33	.787	.261	.128	2.03	6.05	1.45
	10	1.34	.716	.143	.0586	.864	3.65	1.80

environment, the total risk R is the sum over all LET components as (ref. 12)

$$R = \int k_\gamma\Big(L + a_2'L^2 + a_3'L^3 + \ldots\Big)\phi_L\, dL$$

$$= k_\gamma\langle L\rangle\phi + k_\gamma\sum_{i=2}^{n} a_i'\Big\langle L^i\Big\rangle\phi \qquad (38)$$

Here, k_γ is the γ-ray response at the limit of low LET, the zeroth-order moment is the total particle flux, the first-order moment is the locally absorbed dose, and the second-order moment is related to the dose equivalent. A correlation of cell transformation was found in terms of the square of the ratio of the fourth moment to the second moment (ref. 12)

$$p_m(x) = \left[\frac{\big\langle L^4\big\rangle}{\big\langle L^2\big\rangle}\right]^2 \qquad (39)$$

The relative performance index is defined as

$$P_m(x) = \frac{p_{\mathrm{Al}}(x)}{p_m(x)} \qquad (40)$$

The cell-transformation ratio does correlate well with the relative performance index (ref. 12), which is shown with the five lowest moments of LET in table 3. The material dependence of cell transformation is characteristic of the higher LET moments, and a relative performance index is proposed (ref. 12) for evaluation of GCR shield materials. The cell-transformation ratio is shown as a function of areal density for different shields and is relative to the aluminum standard in figure 15. The comparison of cell-transformation ratios for liquid hydrogen, lithium hydride, and lead is shown in figure 15. In this figure, the cell-transformation ratio for liquid hydrogen shows a linear relationship to its areal density x with a best fit of

$$\frac{T_{\mathrm{Al}}(x)}{T_{\mathrm{H_2}}(x)} = 1 + 0.383976x \qquad (41)$$

The ratio has an exponential relationship to x with a best fit of

$$\frac{T_{\mathrm{Al}}(x)}{T_{\mathrm{LiH}}(x)} = \exp\Big(0.07176x - 0.0014999x^2\Big) \qquad (42)$$

for lithium hydride and

$$\frac{T_{\mathrm{Al}}(x)}{T_{\mathrm{Pb}}(x)} = \exp\Big(-0.08366x + 0.001965x^2\Big) \qquad (43)$$

for lead. The liquid hydrogen shows great promise as a high-performance shield material with an increasing shield depth x. This value can provide the relative performance index for all shield materials because of the excellent linearity between the cell-transformation ratio and the relative performance index (ref. 12). We can only presume that such an advantage applies to astronaut exposure risks but must await a clearer understanding of the essential radiobiological factors. Furthermore, the required nuclear cross sections are uncertain and must await further development of the nuclear database and validation

of the shielding codes. This must be accomplished through experimentation at high-energy heavy ion accelerator facilities.

Nuclear Attenuation and Shield Performance

The analysis of shield performance in prior sections has been cast in terms of the microscopic fluctuations of the energy deposit in the exposed biological systems. The range of such fluctuations is determined by the particle type and energy. (See fig. 1.) Relating any particular LET interval with any particular species of the radiation field or to the specific nuclear processes by which the field composition is altered is difficult. The nuclear data are represented by two aspects as they affect the radiation field. The first aspect is the mean free paths of individual species to a nuclear reaction site given in figure 8, and the second aspect is the array of secondary products of the reactions as given in figure 9.

The nuclear free paths are among the best-known nuclear parameters. Although the physical measurements of free paths are limited in the number of projectile-target combinations and beam energies, theoretical calculations can be made without a detailed knowledge of the nuclear excitation spectra and corresponding wave functions because free paths are calculated from the elastic channel amplitudes and are little affected by coupling to inelastic processes (ref. 31). Confidence is gained in that the limited experimental nuclear-absorption cross sections agree well with theoretical calculation (ref. 32).

In distinction, the nuclear breakup depends on the details of the nuclear excitation spectra (both discrete and continuous) and theoretical calculations are not possible (with the exception of very light nuclei). Fortunately, the charge distribution of any particular fragment mass is dominated by the nuclear binding and not so much by the means by which the fragments are produced. Such charge distributions for proton-induced reactions have been studied extensively by Rudstam (ref. 33). The mass-removal cross section could be estimated by a semiempirical liquid drop model in which the surface energy has an empirical correction for highly misshapen nuclei (ref. 34). The semiempirical correction is adjusted to fit the available experimental data, but because of the paucity of experimental data, the validity of this model is in question. Current estimates are shown in figure 9.

In viewing the nuclear free paths in figure 8, the hydrogen shield clearly presents the greatest cross section per unit mass. In addition, the lighter mass shields are more effective in reacting with the heavier ions. Still, the fragment distributions produced also affect the results as shown by Shinn, Townsend, and Wilson (ref. 30).

The effects of the fragment distributions can be studied by looking at the physical limits of the fragmentation event. These limits are expressed as an extreme peripheral collision in which a single nucleon is removed per collision to extreme central collisions in which the nucleus is completely dissociated into nucleonic components. The effects of these physical limits on several shield types are shown in figure 16. The uncertainty in the nuclear fragmentation events has a great effect on the transformation rates of the C3H10T1/2 cell system. This uncertainty is undoubtedly due to the dependence of the transformation rates on the higher moments of the LET distribution that are sensitive to the distribution of fragments produced in the nuclear events (ref. 12).

Although the LET distribution is closely related to the energy fluctuation within specific target sites in the tissue system, LET is not directly related to particle type and, thus, relating the LET distribution to the fragmentation process is difficult. An alternate means of representing the biological response data is to use contributions of biological change from each charge group of the environment as shown in figure 17.

Figure 17 clearly shows that the efficiency of the liquid hydrogen shield comes from its rapid attenuation of the HZE components. For example, the iron flux in free space accounts for nearly 30 percent of the cell transformations, and this flux is reduced by several orders of magnitude in the 30 g/cm^2 liquid hydrogen shield compared with a reduction factor of only 3 behind an equivalent mass of lead shielding. In the liquid hydrogen shield, all components are attenuated to some degree, whereas in the lead shield, the light ions tend to increase as the heavier ions slowly attenuate. In addition, the neutron, hydrogen ions, and helium ions are greatly enhanced over their free-space values, partly because of the secondary production from the target nuclei. These charge distributions are intimately related to the reduction of the high-LET moments and are closely related to the shield parameters studied in laboratory experiments with HZE beams. Clearly, hydrogen-bearing materials will play an important role in shielding from long-term space exposure. In the next section, we examine several possible choices in space construction and begin an evaluation of their effectiveness.

Table 4. Values of Atomic Parameters for Pure Epoxy With $\rho = 1.32$ g/cm^3

Parameter	Hydrogen	Carbon	Nitrogen	Oxygen	Sulfur
Atomic number, Z	1	6	7	8	16
Mass number, A	1	12	14	16	32
Number of atoms in each repeat unit	42	37	4	6	1
Weight in each repeat unit	42	444	56	96	32
Atom density, 10^{22} atoms/gm	3.77	3.32	0.37	0.54	0.09

Table 5. Values of Atomic Parameters for Lunar Regolith With $\rho = 1.5$ g/cm^3

Parameter	Oxygen	Silicon	Aluminum	Iron	Magnesium
Atomic number, Z	8	14	13	26	12
Mass number, A	16	28	27	56	24
Normalized weight, percent	44.7	24.5	9.3	15.4	6.0
Atom density, 10^{21} atoms/gm	16.8	5.28	2.05	1.67	1.50

Table 6. Values of Atomic Parameters for Lunar-Regolith/Epoxy Composites With $\rho_f = 1.5$ g/cm^3 and $\rho_e = 1.32$ g/cm^3

Atomic parameters			Atomic density, 10^{21} atoms/gm, for—	
Elements	Atomic number, Z	Mass number, A	$W_t = 0.1$ epoxy; $\rho_c = 1.48$ g/cm^3	$W_t = 0.2$ epoxy; $\rho_c = 1.46$ g/cm^3
H	1	1	3.78	7.53
C	6	12	3.32	6.65
N	7	14	.359	.72
O	8	16	.539	19.57
S	16	32	.09	.179
Si	14	28	3.74	3.32
Al	13	27	1.51	1.34
Fe	26	56	.59	.525
Mg	12	24	1.24	1.10

Potential Materials for Space Construction

The calculation is extended herein to more complex polymer molecular structures that are hydrogen containing and which may be fabricated and supplied as shield media. The model (ref. 35) of tetraglycidyl 4,4′ diamino diphenyl methane (TG 4,4′ DDM) epoxy that is cured with diamino diphenyl sulfone (DDS) is among those considered. Figure 18 shows this epoxy model, in which the dashed line encloses the cured repeat unit. Table 4 contains the values of the atomic parameters for the pure epoxy with a density (ρ) of 1.32 g/cm^3.

For more specific extended-duration lunar missions, a lunar-soil model by Nealy, Wilson, and Townsend (ref. 36) is used to predict the fluxes of energetic galactic cosmic rays in the internal environment after passing through the thick regolith shield for the protection of the lunar inhabitant. In the case of a lunar-soil model, the five most abundant elements, comprising up to 99.9 percent of the regolith samples, are chosen. The lunar-soil composition, which is normalized to the measured abundances of SiO_2, Al_2O_3, FeO, and MgO, has the elemental percentages given by Nealy, Wilson, and Townsend (ref. 36). Table 5, which contains the values of atomic parameters for lunar regolith with an average soil mass density of 1.5 g/cm^3, is used based on the density range reported of 0.8 to 2.15 g/cm^3. Table 6 contains the values of atomic parameters for lunar-regolith/epoxy composites.

The properties of one group of condensation polymers, the aromatic polyetherimides, are well known. These materials have an unusually high melting

Table 7. Values of Atomic Parameters for Polyetherimide, Polysulfone, and Polyimide

Polymers	Atomic parameters			Atom density, 10^{22} atoms/gm	Density, g/cm^3
	Elements	Atomic number, Z	Mass number, A		
Polyetherimide	H	1	1	2.44	
	C	6	12	3.76	
	N	7	14	.203	1.27
	O	8	16	.61	
Polysulfone	H	1	1	3.0	
	C	6	12	3.68	
	O	8	16	.545	1.24
	S	16	32	.136	
Polyimide	H	1	1	1.58	
	C	6	12	3.47	
	N	7	14	.315	1.42
	O	8	16	.788	

point, are easy to process, and possess outstanding thermal stabilities. The commercial polyetherimide Ultem from the General Electric Company (ref. 37) is evaluated as a shield material.

Many polyethers are amorphous, rigid, tough thermoplastics with high second-order transitions, glass transition temperatures (T_g), and noteworthy electrical properties. One of the aromatic polyethers, polysulfone Udell P-1700 (ref. 38) from the Union Carbide Corporation, is also investigated for shielding.

Aromatic polypyromellitimides are materials with excellent thermal, oxidative, and hydrolytic stability. One of the polyimides from the Du Pont Corporation, the thermoset Kapton, is also investigated as a shield material. Films of the aromatic polypyromellitimides with a thickness of 2.0 mils have shown outstanding resistance to irradiation from high-energy electrons and from thermal neutrons (ref. 39). Table 7 contains the values of the atomic parameters for polyetherimide, polysulfone, and polyimide, and the repeat units of these polymers are shown in figure 19.

The addition of boron powder to a polymer allows the material to absorb low-energy neutrons (ref. 40) because neutrons have a high probability of reacting with a nucleus in a process called neutron capture when the neutrons have been slowed down to very low energies. Neutron thermalization is a natural consequence of transport through the hydrogen-bearing polymers. Low-energy neutrons react with a stable isotope of boron (^{10}B), which constitutes 19.6 percent of the naturally occurring element. The products of the reaction, ^{4}He and ^{7}Li, are not radioactive. Thus, various weight fractions of boron in films of these polymers are studied to compare their neutron-absorbing capability. Natural boron, which has an atomic number (Z) of 5, is used in the form of an amorphous submicron powder with a density of 2.59 g/cm^3. Table 8 contains the values of the atomic parameters for the polymer-boron composites. We next evaluate the effects of the shield composition on the astronaut environment and ultimately on astronaut risk.

Experimental and Theoretical Studies

With the straight-ahead approximation and the target secondary fragments neglected, the transport equation is written as (refs. 1 and 2)

$$\left(\frac{\partial}{\partial x} - \frac{\partial}{\partial E}\widetilde{S}_j + \sigma_j\right)\phi_j(x,E) = \sum_{k\geq j} m_{jk}\sigma_k\,\phi_k(x,E) \tag{44}$$

where

$\phi_j(x,E)$ flux of ions of type j with atomic mass A_j at x moving along x-axis at energy E (in units of MeV/amu)

σ_j corresponding macroscopic nuclear absorption cross sections

$\widetilde{S}_j$ change in E per unit distance

m_{jk} fragmentation parameter for ion j produced in collision by ion k

The primary beams were taken as ^{56}Fe at 605 MeV/amu or ^{20}Ne at 425 MeV/amu. An initial range for the primary ion beam for a material with known density is calculated by using the

Table 8. Values of Atomic Parameters for Various Polymers Containing Boron and Hydrogen

Polymers	Atomic parameters			Atom density, 10^{22} atoms/gm, for—			
	Elements	Atomic number, Z	Mass number, A	5 percent B	10 percent B	15 percent B	20 percent B
Polyetherimide	H	1	1	23.2	22.0	20.7	19.5
	C	6	12	35.8	33.8	32.0	30.1
	N	7	14	1.93	1.83	1.73	1.63
	O	8	16	5.80	5.49	5.18	4.88
	B	5	11	2.23	4.46	6.69	8.93
	B	5	10	.558	1.11	1.67	2.23
Polysulfone	H	1	1	28.6	27.0	25.5	24.1
	C	6	12	35.0	33.1	31.3	29.6
	O	8	16	5.19	4.90	4.63	4.38
	S	16	32	1.30	1.22	1.16	1.10
	B	5	11	2.11	4.46	6.66	8.76
	B	5	10	.527	1.12	1.66	2.20
Polyimide	H	1	1	15.0	14.2	13.4	12.6
	C	6	12	33.0	31.2	29.4	27.7
	N	7	14	3.0	2.84	2.67	2.52
	O	8	16	7.52	7.10	6.69	6.31
	B	5	11	2.15	4.46	6.82	8.9
	B	5	10	.538	1.12	1.7	2.23

Bethe formula where the linear energy transfer per unit mass $\widetilde{S}_j$ is quite accurate at high energy. The solution (ref. 41) to equation (44) is

$$\phi_j(x,E) = \phi_j^{(0)}(x,E) + \phi_j^{(1)}(x,E) + \phi_j^{(2)}(x,E) \quad (45)$$

where $\phi_j^{(0)}(x,E)$ is the attenuated primary ion fluence, $\phi_j^{(1)}(x,E)$ is the first collision term, and $\phi_j^{(2)}(x,E)$ is the second collision term. The results of the first collision term $\phi_j^{(1)}(x,E)$ and of the second collision term $\phi_j^{(2)}(x,E)$ are integrated numerically over their entire energy spectrum.

The total integral flux associated with each term is evaluated as

$$\Phi_j^{(1)}(x) = \int_0^\infty \phi_j^{(1)}(x,E)\,dE \approx \sum_i \phi_j^{(1)}(x,E_i)\,(\Delta E) \quad (46)$$

and

$$\Phi_j^{(2)}(x) = \int_0^\infty \phi_j^{(2)}(x,E)\,dE \approx \sum_i \phi_j^{(2)}(x,E_i)\,(\Delta E) \quad (47)$$

For a three-term perturbation expansion, the total ion fluence is

$$\Phi_j(x) = \Phi_j^{(0)}(x) + \Phi_j^{(1)}(x) + \Phi_j^{(2)}(x) \quad (48)$$

To compare the flux of each identified nucleus with charge Z, $\phi_z(x,E)$ is defined as

$$\phi_z(x,E) = \sum_{A_j} \phi_{z,A_j}(x,E) \quad (49)$$

where $\phi_{z,A_j}(x,E)$ is the same as $\phi_j(x,E)$ of equation (45) for all the isotopes of projectile fragment charge Z with different atomic mass A_j. Equation (49) is integrated numerically over the entire energy spectrum and the total integral flux for each charge Z is approximated as

$$\Phi_z(x) = \int_0^\infty \phi_z(x,E)\,dE \approx \sum_i \phi_z(x,E_i)\,(\Delta E) \quad (50)$$

The high-energy heavy ion radiation components are usually attenuated to lower LET as a result of nuclear interactions between projectile and target nuclei, and these processes become more significant as the particles penetrate further into the shield medium. Recall that LET is proportional to the

Table 9. Calculated Initial Range for Different Polymeric Materials

Polymers	ρ, g/cm^3	Initial range of ^{56}Fe beam at 605 MeV/amu, g/cm^2	Initial range of ^{20}Ne beam at 425 MeV/amu, g/cm^2
Pure polyetherimide	1.27	13.8	19.2
5 percent B	1.30	13.9	19.3
10 percent B	1.33	14.0	19.5
15 percent B	1.36	14.0	19.6
20 percent B	1.40	14.1	19.7
Pure polysulfone	1.24	13.7	19.1
5 percent B	1.27	13.8	19.2
10 percent B	1.30	13.9	19.3
15 percent B	1.34	14.0	19.5
20 percent B	1.37	14.0	19.5
Pure polyimide	1.42	14.1	19.6
5 percent B	1.45	14.1	19.7
10 percent B	1.48	14.2	19.8
15 percent B	1.51	14.3	19.9
20 percent B	1.54	14.4	20.0
Polyethylene		12.2	
Poly(tetrafluoroethylene)		15.7	

square of the ion charge. The internal environment within the spacecraft or habitat structure that interacts with onboard personnel or equipment depends on the shield composition resulting from the differences in atomic cross sections, nuclear attenuation, and the distribution of fragmentation products. In preparation of experimental studies of the attenuation of ion beams in potential space construction materials, theoretical predictions based on current understanding are used as a guide to an experimental program. In the following calculations, the fragmentation cross sections of Silberberg, Tsao, and Shapiro (ref. 42) were used in that they were the only database available for these codes at the time of use.

The initial range of penetration of a 605-MeV/amu ^{56}Fe beam in lunar regolith with a density of 1.5 g/cm^3 is approximately 10 cm (15.4 g/cm^2). The calculations show (see fig. 20) that lighter particles with energies lower than 605 MeV/amu are predicted to be in relative abundance for a lunar-regolith brick with a thickness of 16 g/cm^2, which is slightly larger than the range of 15.4 g/cm^2. Note that the addition of hydrogen-bearing epoxy to the regolith brick increases the protection. Figure 21 shows that the lighter particles with energies lower than 605 MeV/amu are also predicted to be in abundance for a lunar-regolith brick with a thickness of 18 g/cm^2. These results demonstrate that most of these particles are secondaries from the nuclear interaction processes. Most conspicuous is that the maximum contribution comes from a broad range of charges above $Z = 3$ (for Li).

The calculated initial ranges of the primary ^{56}Fe beam at 605 MeV/amu and of the ^{20}Ne beam at 425 MeV/amu for each polymer are shown in table 9. From these calculated initial ranges, a 10 g/cm^2 thickness is considered to be a thin target and an 18 g/cm^2 thickness is a thick target for a primary ^{56}Fe beam at 605 MeV/amu, whereas an 18 g/cm^2 thickness is considered to be a thin target for a primary ^{20}Ne beam at 425 MeV/amu. The fluences of identified projectile fragment nuclei are compared for 18 g/cm^2 thick targets for the primary ^{56}Fe beam at 605 MeV/amu and for 20 g/cm^2 thick targets for the primary ^{20}Ne beam at 425 MeV/amu where the thicknesses are slightly larger than the initial ranges.

Because of the greater hydrogen content of polyethylene, the charge difference in fragmentation by polyethylene is smaller than that by poly(tetrafluoroethylene) and other polymers. However, thin

polyethylene enhances the high Z fragment. The second fragmentation event occurs more often in the thicker polyethylene shields because the nuclear attenuation rate is higher in polyethylene than in the other polymer shields. The second charge difference greatly reduces the fluence for a polyethylene shield (ref. 30).

The lighter material such as polyethylene enhances the high-energy heavy ion fluence relative to poly(tetrafluoroethylene) for thin shields (see fig. 22) and reduces the fluence more efficiently than poly(tetrafluoroethylene) and other polymers for thick shields (see fig. 23). In fact, the succession of curves in figures 22 and 23 is governed by the amount of hydrogen per unit mass, and polyethylene is the most abundant in hydrogen. Studies on the effect of shield composition on LET distribution at several depths has already shown that polyethylene is the most effective high-LET degrader beyond 5 g/cm^2 at solar minimum (ref. 30). Again, polyethylene is the most effective shield material among these polymers beyond an 18 g/cm^2 thickness for the primary ^{56}Fe beam at 605 MeV/amu.

The addition of boron (B) powder to a material allows the material to absorb low-energy neutrons without any degradation in glass transition temperature or Young's modulus in the polymeric materials (ref. 40). The fluence for a polyetherimide containing various weight fractions of boron is shown in figure 24 for a primary ^{56}Fe beam at 605 MeV/amu and in figure 25 for a primary ^{20}Ne beam at 425 MeV/amu. These results show no significant difference for various weight fractions of boron. For thick shields, the pure polymer shows a slightly better attenuation of fragments at $Z > 3$ than a composite containing 20 percent boron. As the fraction of B increases from 5 to 20 percent by weight, both the density and the initial range increase because boron has a higher atomic number (Z) than hydrogen. Similar results are obtained for the polysulfone and the polyimide. Hence, pure polymers with slightly shorter initial ranges are expected to attenuate fragments at $Z > 3$ better than materials containing any fraction of boron. The laboratory code used does not include light fragments of $Z < 3$ in any realistic way because a greater knowledge of nuclear fragmentation processes and a corresponding transport theory are required for these fragments.

A target with a high percentage of lighter atoms such as hydrogen would, therefore, be an effective shield material for thick shields, whereas a target with a heavier atom composition might yet prove to be more effective in thin shields for energetic ion beams. Pilot experiments to validate these theoretical results have been performed, but data reduction is not yet complete.

Concluding Remarks

Radiation risks to astronauts depend on the microscopic fluctuations of energy-absorption events in specific tissues. These fluctuations depend not only on the space environment but also on the modifications of that environment by the shielding of the astronaut's surrounding structures and the attenuation characteristics of the astronaut's body. The effects of attenuation of the shield and body depend on the tissue biological response to the microscopic fluctuation effects. A great deal of uncertainty presently exists in estimating astronaut risk because of uncertainty in the nuclear properties and risk models. Clearly, these uncertainties must be reduced before the shield design can be made.

Using current estimates for nuclear cross sections has shown that the high charge and energy (HZE) ions in space pose a significant hazard to biological systems and that the linear energy transfer (LET) distribution above about 10 keV/μm is an important indicator of biological damage. Furthermore, the LET distribution is a function of shield composition, even with materials of the same areal density. Shinn et al. suggested that polyethylene with its short nuclear absorption lengths is an effective shield material in spite of the favoring of massive projectile fragments, and this has been demonstrated herein for monoenergetic ion beams. The establishment of a reliable nuclear fragmentation database, astronaut risk methodology, suitable polymer materials, and structural design methods remain as critical issues in the long-term exposure to space radiations.

NASA Langley Research Center
Hampton, VA 23681-0001
August 29, 1994

References

1. Wilson, John W.: Environmental Geophysics and SPS Shielding. *Workshop on the Radiation Environment of the Satellite Power System*, Walter Schimmerling and Stanley B. Curtis, eds., LBL-8581 (Contract W-7405-ENG-48), Univ. of California, Sept. 15, 1978, pp. 33–116.

2. Wilson, John W.; Townsend, Lawrence W.; Schimmerling, Walter; Khandelwal, Govind S.; Khan, Ferdous; Nealy, John E.; Cucinotta, Francis A.; Simonsen, Lisa C.; Shinn, Judy L.; and Norbury, John W.: *Transport Methods and Interactions for Space Radiations*. NASA RP-1257, 1991.

3. *Guidance on Radiation Received in Space Activities*. NCRP Rep. No. 98, National Council on Radiation Protection and Measurements, 1989.

4. Schaefer, Hermann J.: Evaluation of Present-Day Knowledge of Cosmic Radiation at Extreme Altitude in Terms of the Hazard to Health. *J. Aviation Med.*, vol. 21, no. 5, Oct. 1950, pp. 375–394, 418.

5. Tobias, Cornelius A.: Radiation Hazards in High Altitude Aviation. *J. Aviation Med.*, vol. 23, no. 4, Aug. 1952, pp. 345–372.

6. Schimmerling, Walter: Radiobiological Problems in Space—An Overview. *Radiat. & Environ. Biophys.*, vol. 31, 1992, pp. 197–203.

7. *1990 Recommendations of the International Commission on Radiological Protection.* ICRP Publ. 60, Pergamon Press Inc., 1991.

8. Committee on the Biological Effects of Ionizing Radiations: *Health Effects of Exposure to Low Levels of Ionizing Radiation.* BEIR V, National Academy Press, 1990.

9. Aghamohammadi, S. Z.; Goodhead, D. T.; and Savage, J. R.: Induction of Sister Chromatid Exchanges (SCE) in GO Lymphocytes by Plutonium-238 Alpha-Particles. *Int. J. Radiat. Biol. & Relat. Stud. Phys., Chem. & Med.*, vol. 53, no. 6, June 1988, pp. 909–915.

10. Kadhim, M. A.; Macdonald, D. A.; Goodhead, D. T.; Lorimore, S. A.; Marsden, S. J.; and Wright, E. G.: Transmission of Chromosomal Instability After Plutonium α-Particle Irradiation. *Nature*, vol. 355, no. 6362, Feb. 20, 1992, pp. 738–740.

11. Kraft, G.: Radiobiological Effects of Very Heavy Ions: Inactivation, Induction of Chromosome Aberrations and Strand Breaks. *Nucl. Sci. Appl.*, sect. A, vol. 3, no. 1, 1987, pp. 1–28.

12. Wilson, John W.; Wood, J. S.; Shinn, Judy L.; Cucinotta, Francis A.; and Nealy, John E.: *A Proposed Performance Index for Galactic Cosmic Ray Shielding Materials.* NASA TM-4444, 1993.

13. Wilson, John W.; Cucinotta, F. A.; and Shinn, J. L.: Cell Kinetics and Track Structure. *Biological Effects and Physics of Solar and Galactic Cosmic Radiation, Part B*, Charles E. Swenberg, Gerda Horneck, and E. G. Stassinopoulos, eds., Plenum Press, 1993, pp. 295–338.

14. Yang, T. C.; and Tobias, C. A.: Neoplastic Cell Transformation by Energetic Heavy Ions and Its Modification With Chemical Agents. *Adv. Space Res.*, vol. 4, no. 10, 1984, pp. 207–218.

15. Yang, Tracy Chui-Hsu; Craise, Laurie M.; Mei, Man-Tong; and Tobias, Cornelius A.: Neoplastic Cell Transformation by High-LET Radiation: Molecular Mechanisms. *Adv. Space Res.*, vol. 9, no. 10, 1989, pp. (10)131–(10)140.

16. Bond, V. P.; Varma, M. N.; and Sondhaus, C. A.: The RBE Concept, Its Inadequacies and a Suggested Replacement. *Mechanisms of Radiation Interaction With DNA: Potential Implications for Radiation Protection*, CONF-870163, U.S. Dep. of Energy, 1988, pp. 31–38.

17. Xapsos, M. A.; Burke, E. A.; Shapiro, P.; and Summers, G. P.: Energy Deposition and Ionization Fluctuations Induced by Ions in Small Sites—An Analytical Approach. *Radiat. Res.*, vol. 137, no. 2, Feb. 1994, pp. 152–161.

18. Todd, Paul: Unique Biological Aspects of Radiation Hazards—An Overview. *Adv. Space Res.*, vol. 3, no. 8, 1983, pp. 187–194.

19. *The Quality Factor in Radiation Protection.* ICRU Rep. 40, International Commission on Radiation Units and Measurements, Apr. 4, 1986.

20. Scott, B. R.: Methodologies for Predicting the Expected Combined Stochastic Radiobiological Effects of Different Ionizing Radiations and Some Applications. *Radiat. Res.*, vol. 98, no. 1, Apr. 1984, pp. 182–197.

21. Burns, F. J.; and Albert, R. E.: Dose-Response for Radiation-Induced Cancer in Rat Skin. *Radiation Carcinogenesis and DNA Alterations,* F. J. Burns, A. C. Upton, and G. Silini, eds., Plenum Press, 1986, pp. 51–70.

22. Thomson, John F.; and Grahn, Douglas: Life Shortening in Mice Exposed to Fission Neutrons and γ Rays. VII. Effects of 60 Once-Weekly Exposures. *Radiat. Res.*, vol. 115, 1988, pp. 347–360.

23. Wilson, John W.; Nealy, John E.; Schimmerling, Walter; Cucinotta, Francis A.; and Wood, James S.: *Effects of Radiobiological Uncertainty on Vehicle and Habitat Shield Design for Missions to the Moon and Mars.* NASA TP-3312, 1993.

24. Katz, R.; Ackerson, B.; Homayoonfar, M.; and Sharma, S. C.: Inactivation of Cells by Heavy Ion Bombardment. *Radiat. Res.*, vol. 47, 1971, pp. 402–425.

25. Wilson, John W.; and Cucinotta, Francis A.: *Cellular Repair/Misrepair Track Model.* NASA TP-3124, 1991.

26. Wilson, John W.; Cucinotta, Francis A.; and Shinn, Judy L.: *Multiple Lesion Track Structure Model.* NASA TP-3185, 1992.

27. Wilson, John W.; Chun, Sang Y.; Badavi, Forooz F.; Townsend, Lawrence W.; and Lamkin, Stanley L.: *HZETRN: A Heavy Ion/Nucleon Transport Code for Space Radiations.* NASA TP-3146, 1991.

28. Townsend, L. W.; Cucinotta, F. A.; and Wilson, J. W.: HZE Reactions and Data-Base Development. *Biological Effects and Physics of Solar and Galactic Cosmic Radiation*, 1993, pp. 787–809.

29. Shinn, Judy L.; John, Sarah; Tripathi, Ram K.; Wilson, John W.; Townsend, Lawrence W.; and Norbury, John W.: *Fully Energy-Dependent HZETRN (A Galactic Cosmic-Ray Transport Code).* NASA TP-3243, 1992.

30. Shinn, Judy L.; Townsend, Lawrence W.; and Wilson, John W.: Galactic Cosmic Ray Radiation Levels in Spacecraft on Interplanetary Missions. *Book of Abstracts—The World Space Congress, 43rd Congress of the International Astronautical Federation and 29th Plenary Meeting*

of the Committee on Space Research, International Astronautical Federation and Committee on Space Research, Aug.–Sept. 1992, pp. 567–568.

31. Wilson, John W.: Composite Particle Reaction Theory. Ph.D. Diss., College of William and Mary, June 1975.

32. Wilson, J. W.; and Townsend, L. W.: An Optical Model for Composite Nuclear Scattering. *Canadian J. Phys.*, vol. 59, no. 11, 1981, pp. 1569–1576.

33. Rudstam, G.: Systematics of Spallation Yields. *Zeitschrift fur Naturforschung*, vol. 21a, no. 7, July 1966, pp. 1027–1041.

34. Wilson, John W.; Townsend, Lawrence W.; and Badavi, F. F.: A Semiempirical Nuclear Fragmentation Model. *Nucl. Instrum. & Methods Phys. Res.*, vol. B18, no. 3, Feb. 1987, pp. 225–231.

35. Long, Edward R., Jr.: *Electron and Proton Absorption Calculations for a Graphite/Epoxy Composite Model.* NASA TP-1568, 1979.

36. Nealy, John E.; Wilson, John W.; and Townsend, Lawrence W.: *Solar-Flare Shielding With Regolith at a Lunar-Base Site.* NASA TP-2869, 1988.

37. Johnson, R. N.; Farnham, A. G.; Clendinning, R. A.; Hale, W. F.; and Merriam, C. N.: Poly(aryl Ethers) by Nucleophilic Aromatic Substitution. I. Synthesis and Properties. *J. Polym. Sci.:* pt. A-1, vol. 5, 1967, pp. 2375–2398.

38. White, D. M.; Takekoshi, T.; Williams, F. J.; Relles, H. M.; Donahue, P. E.; Klopfer, H. J.; Loucks, G. R.; Manello, J. S.; Mathews, R. O.; and Schluenz, R. W.: Polyetherimides Via Nitro-Displacement Polymerization: Monomer Synthesis and ^{13}C-NMR Analysis of Monomers and Polymers. *J. Polym. Sci.: Polymer Chemistry Ed.*, vol. 19, 1981, pp. 1635–1658.

39. Sroog, C. E.; Endrey, A. L.; Abramo, S. V.; Berr, C. E.; Edwards, W. M.; and Olivier, K. L.: Aromatic Polypyromellitimides From Aromatic Polyamic Acids. *J. Polym. Sci.*, pt. A, vol. 3, no. 4, Apr. 1965, pp. 1373–1390.

40. Kraus, W. B.; Glasgow, M. B.; Kim, M. Y.; Olmeijer, D. L.; Kiefer, R. L.; Orwoll, R. A.; and Thibeault, S. A.: Boron Containing Polymers for Radiation Shielding. *Polym. Prep.*, vol. 34, no. 1, Mar. 1993, pp. 592–593.

41. Wilson, John W.; Lamkin, Stanley L.; Farhat, Hamidullah; Ganapol, Barry D.; and Townsend, Lawrence W.: *A Hierarchy of Transport Approximations for High Energy Heavy (HZE) Ions.* NASA TM-4118, 1989.

42. Silberberg, R.; Tsao, C. H.; and Shapiro, M. M.: Semiempirical Cross Sections, and Applications to Nuclear Interactions of Cosmic Rays. *Spallation Nuclear Reactions and Their Applications*, B. S. P. Shen and M. Merker, eds., D. Reidel Publ. Co., 1976, pp. 49–81.

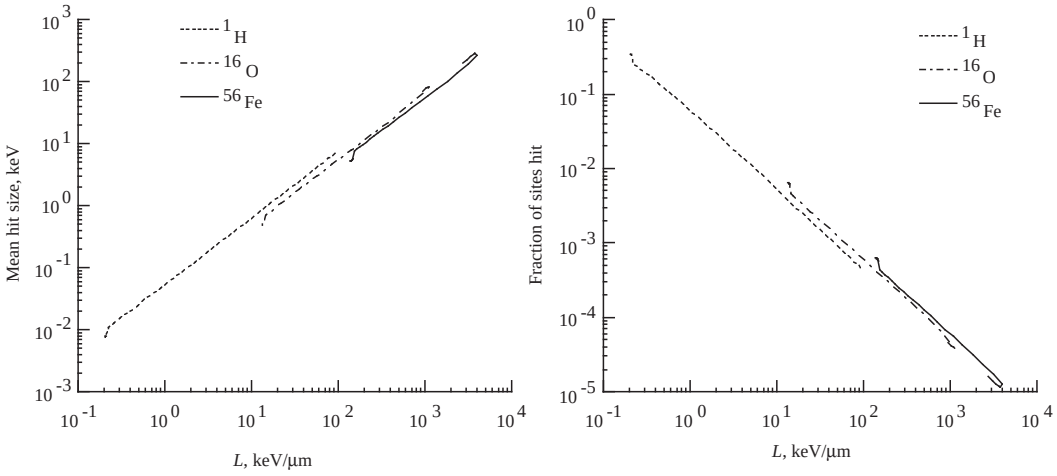

(a) 0.1-μm site size.

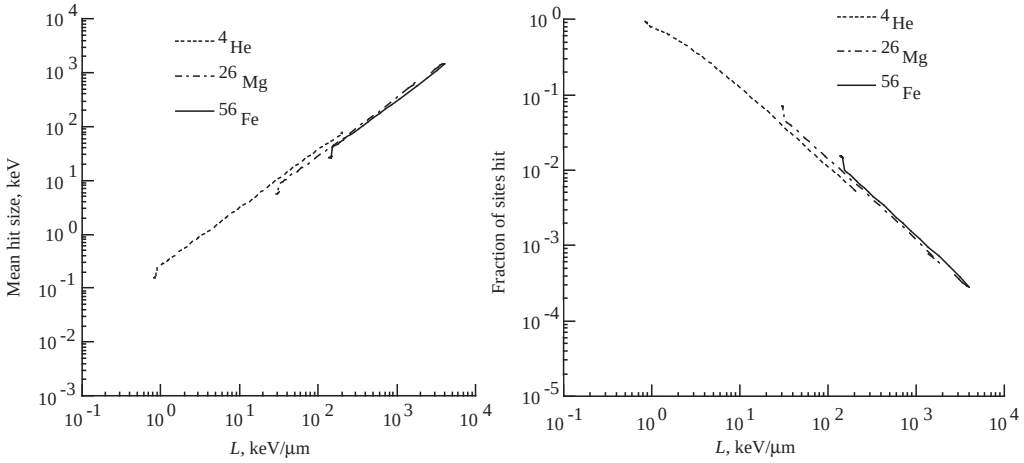

(b) 0.5-μm site size.

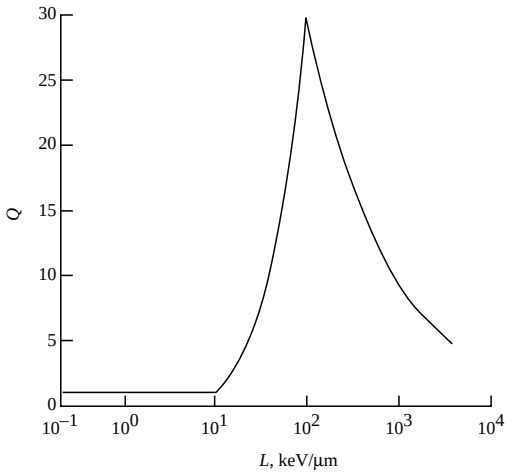

(c) Quality factor.

Figure 1. Fraction of hit sites, hit size, and quality factor as a function of LET (L).

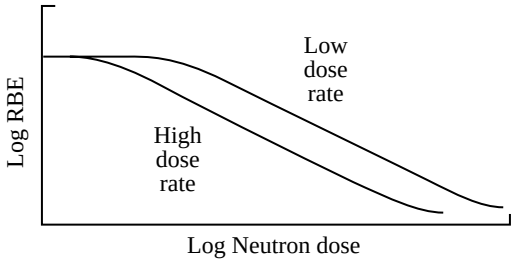

Figure 2. Schematic of RBE for neutron exposure at different dose rates.

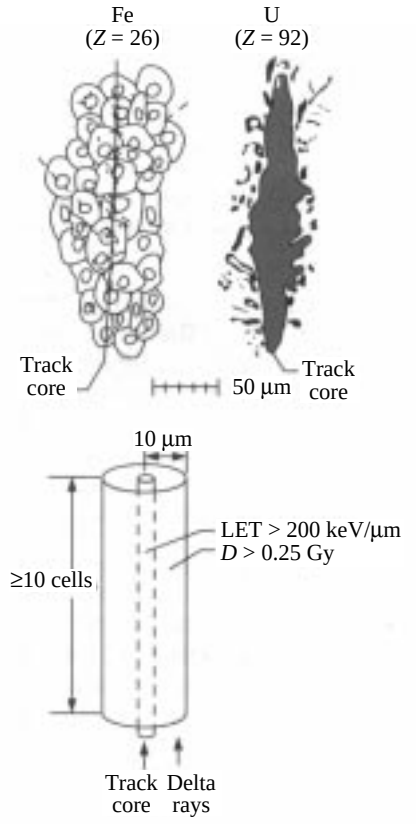

Figure 3. Single-particle effect proposed by Todd (ref. 18).

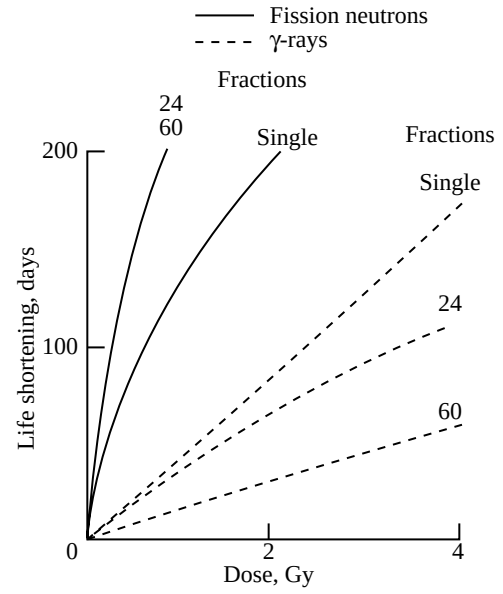

Figure 4. Dose protraction effects in mice with repair for low LET (γ-ray) and enhancement at high LET for fission neutron (ref. 22).

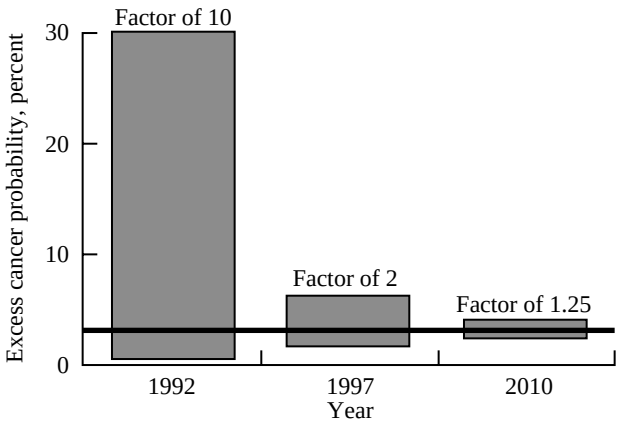

Figure 5. Estimates for current and projected risk uncertainties in NASA Space Radiation Program.

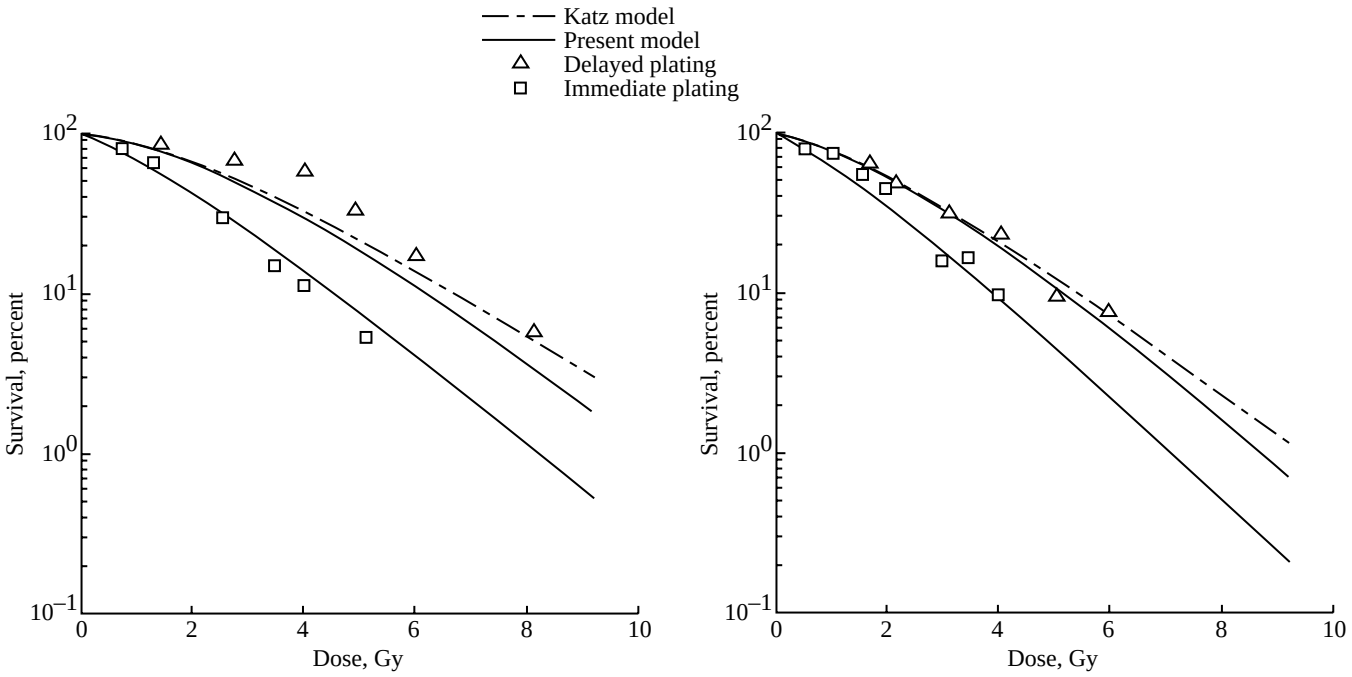

(a) ^{20}Ne with 425 MeV/amu^{-1} at 32 keV/μm.

(b) ^{28}Si with 670 MeV/amu at 50 keV/μm.

(c) ^{28}Si with 320 MeV/amu at 82 keV/μm^{-1}.

(d) ^{56}Fe with 600 MeV/amu at 190 keV/μm.

Figure 6. Cell survival of C3H10T1/2 for delayed plating and immediate plating.

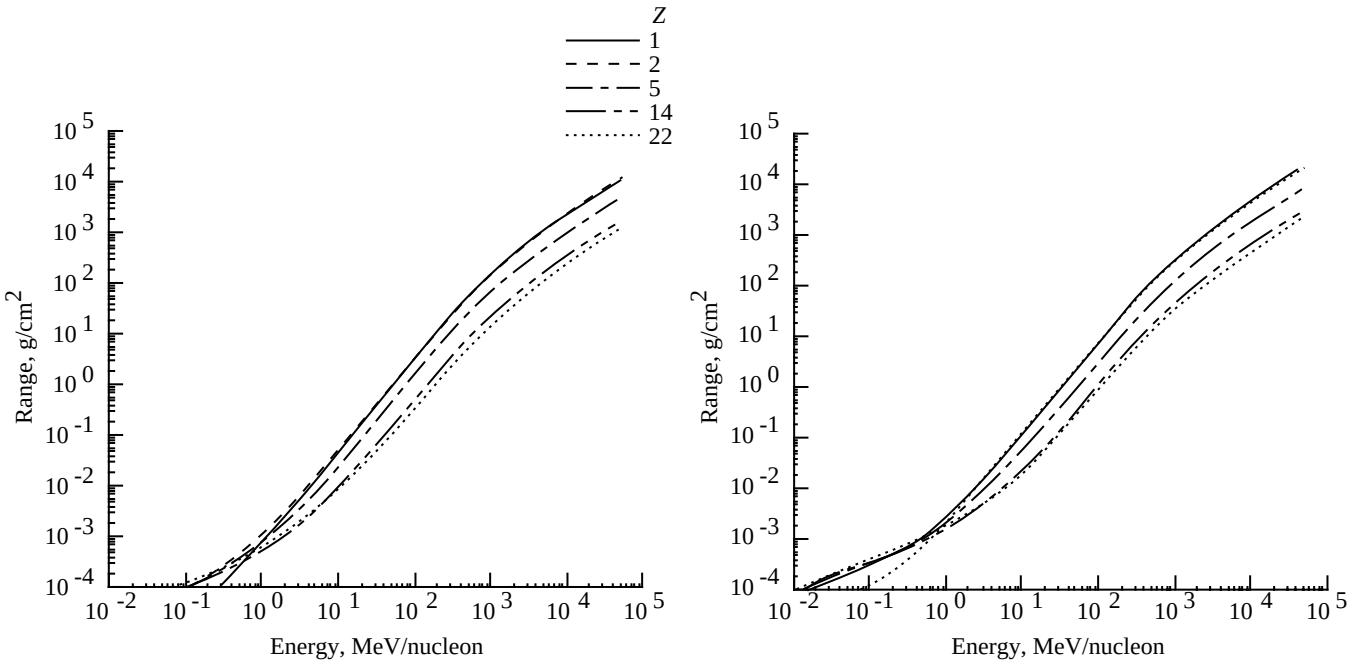

(a) Liquid hydrogen.

(b) Water.

(c) Aluminum.

(d) Lead.

Figure 7. Stopping ranges of selected ions in four diverse materials.

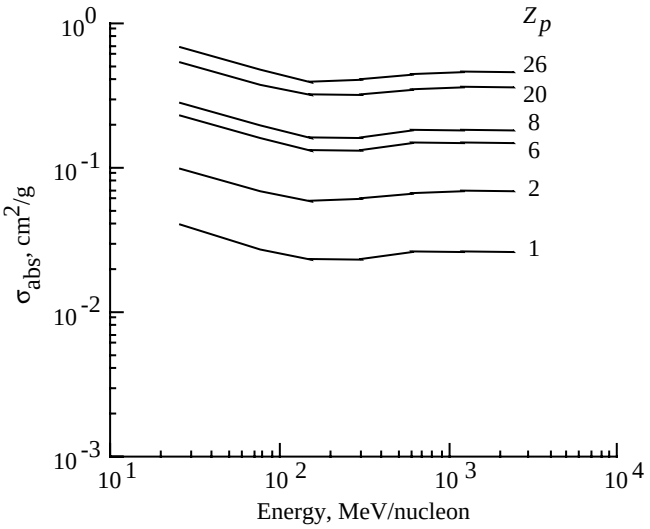

(a) Liquid hydrogen.

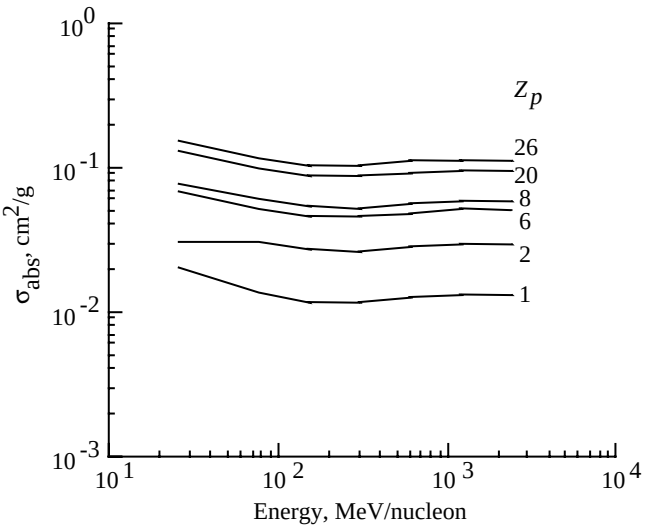

(b) Water.

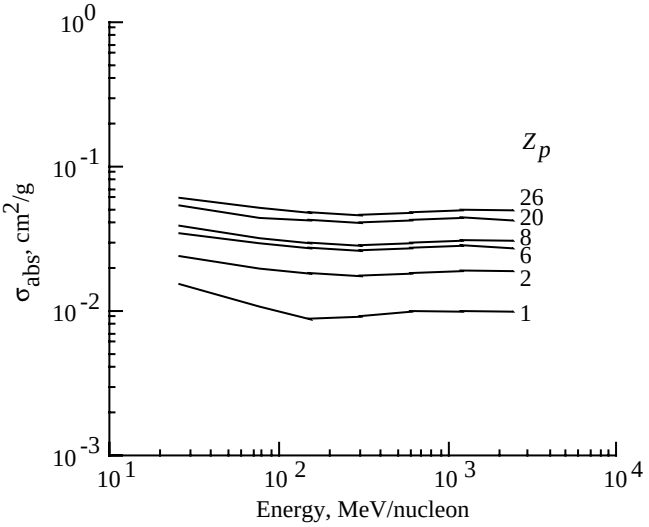

(c) Aluminum.

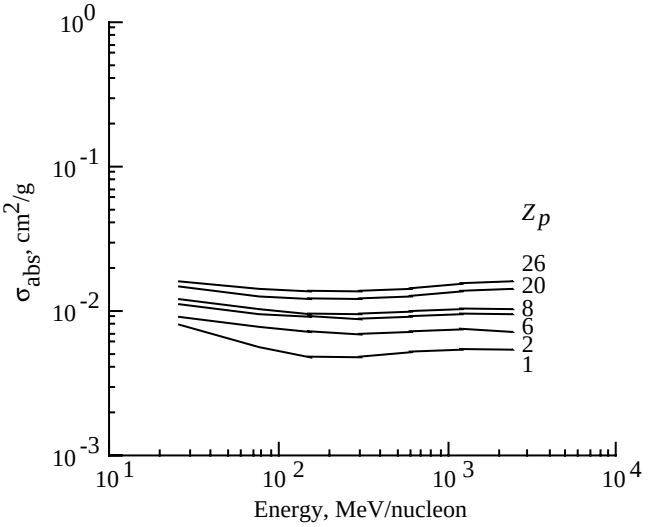

(d) Lead.

Figure 8. Nuclear absorption cross sections per unit mass for selected ions in four diverse materials.

(a) Liquid hydrogen.

(b) Water.

(c) Aluminum.

(d) Lead.

Figure 9. Fragment production cross sections per unit mass for ions transported in the shielding code in four diverse materials.

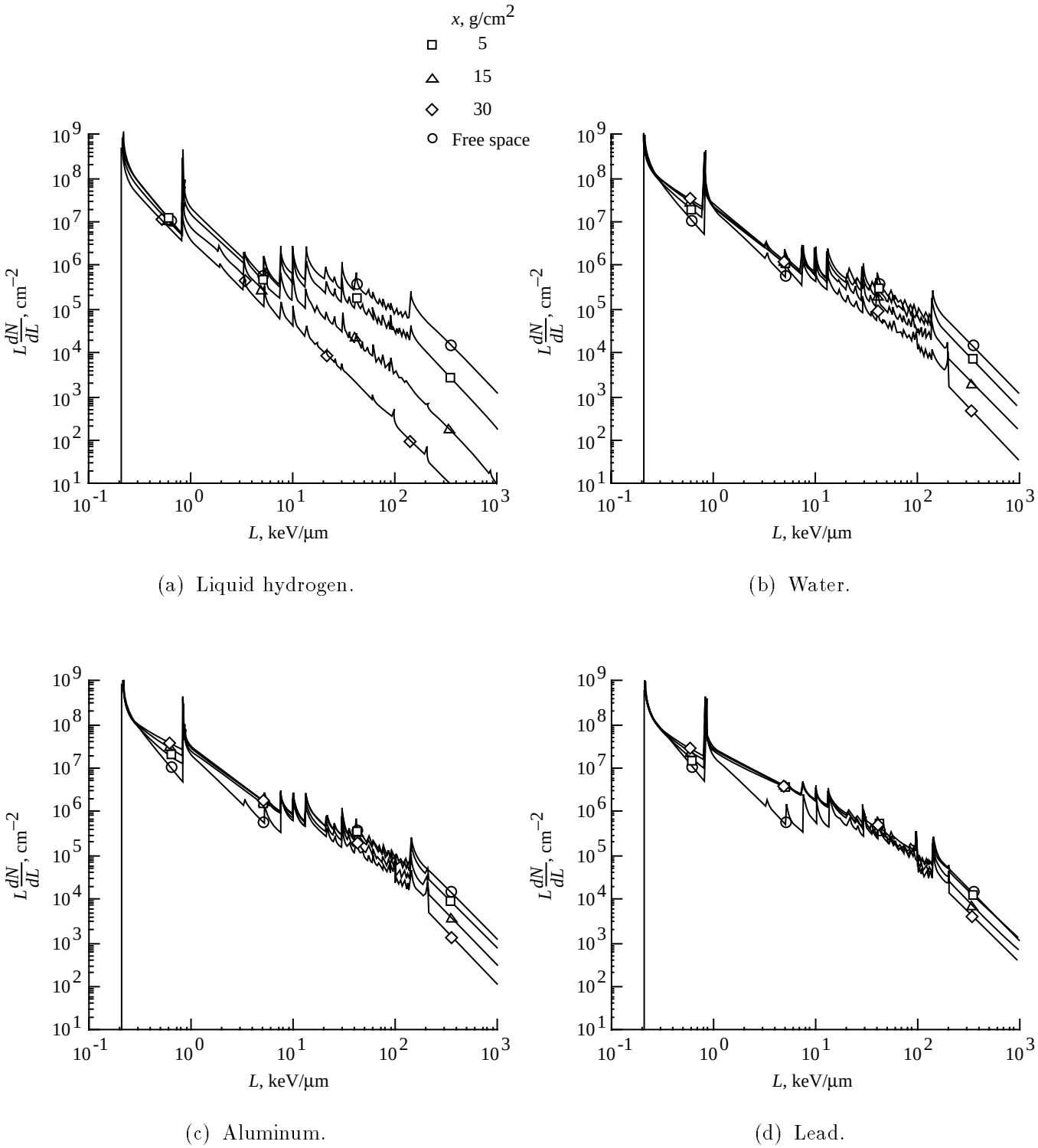

(a) Liquid hydrogen.

(b) Water.

(c) Aluminum.

(d) Lead.

Figure 10. Annual transmitted GCR differential LET spectrum in four diverse shield materials.

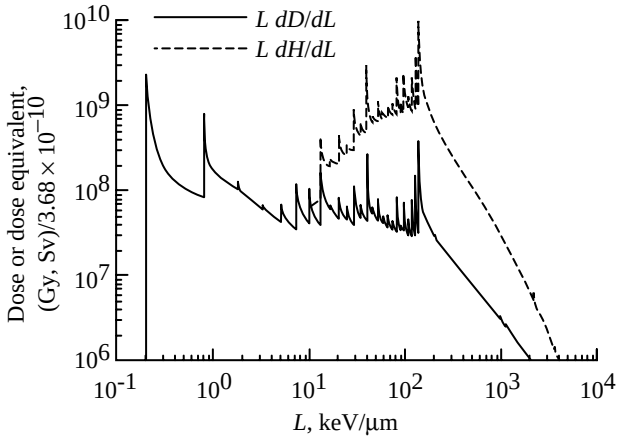

Figure 11. Differential LET spectra for annual dose and dose equivalent with 5-g/cm^2 aluminum shield.

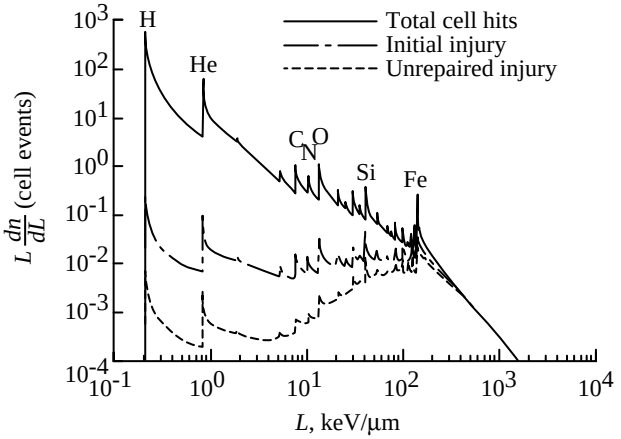

Figure 12. Differential LET contributions to cell events in 1-year exposure behind 5-g/cm^2 aluminum shield.

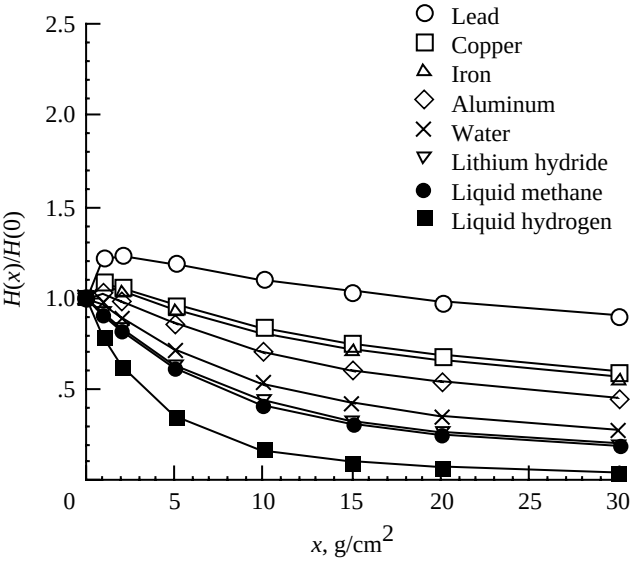

(a) Dose equivalent.

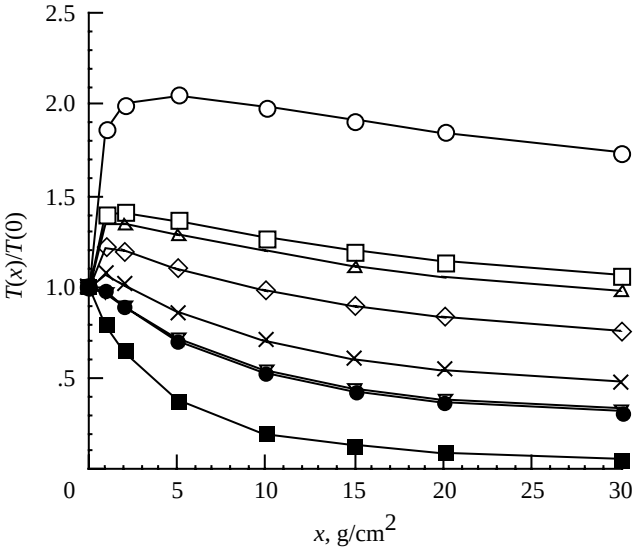

(b) Transformations.

Figure 13. Attenuation of dose equivalent and cell transformation in 1-year exposure behind several shield materials.

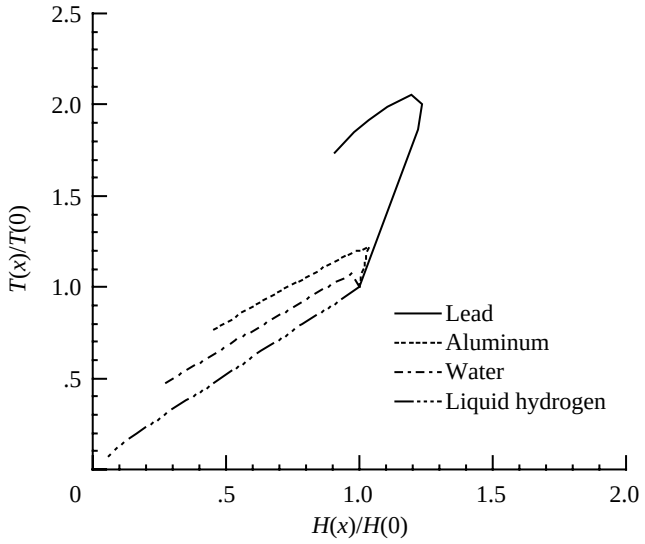

Figure 14. Correlation of cell transformation and dose equivalent behind several shield materials.

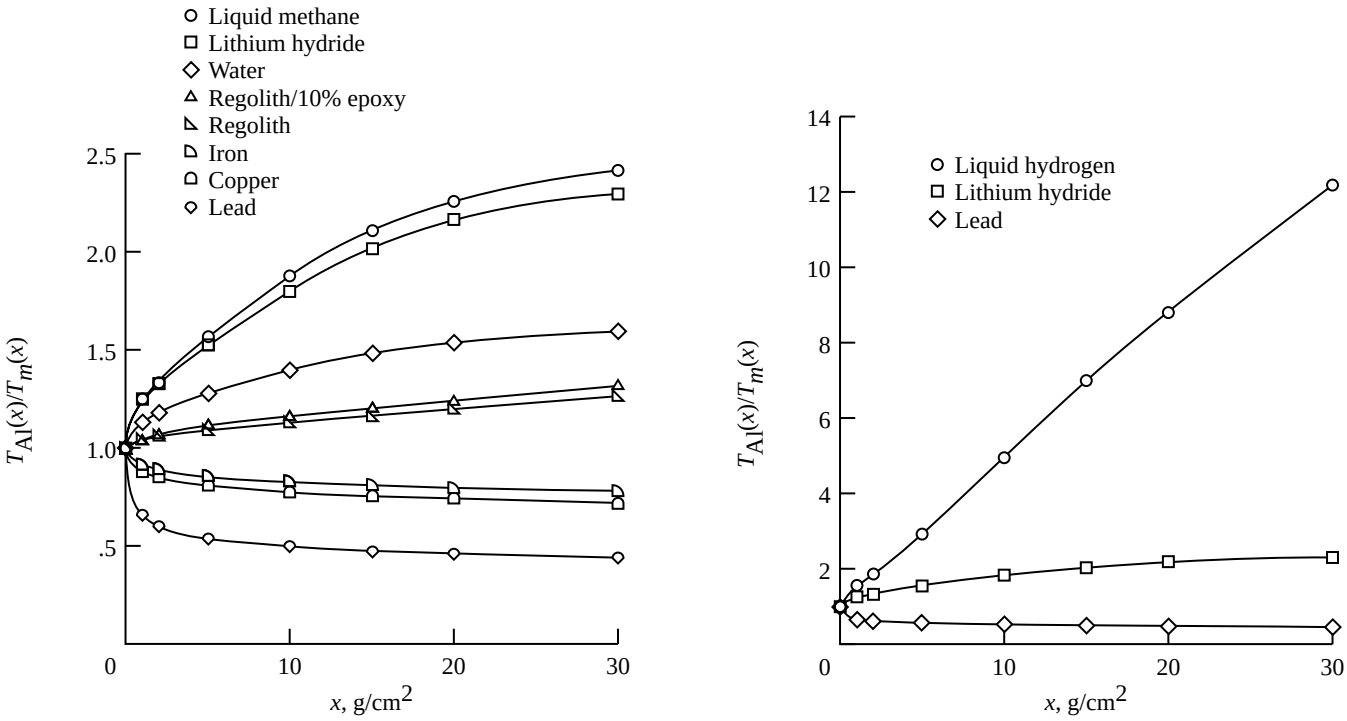

Figure 15. Cell-transformation ratio as a function of areal density relative to aluminum standard.

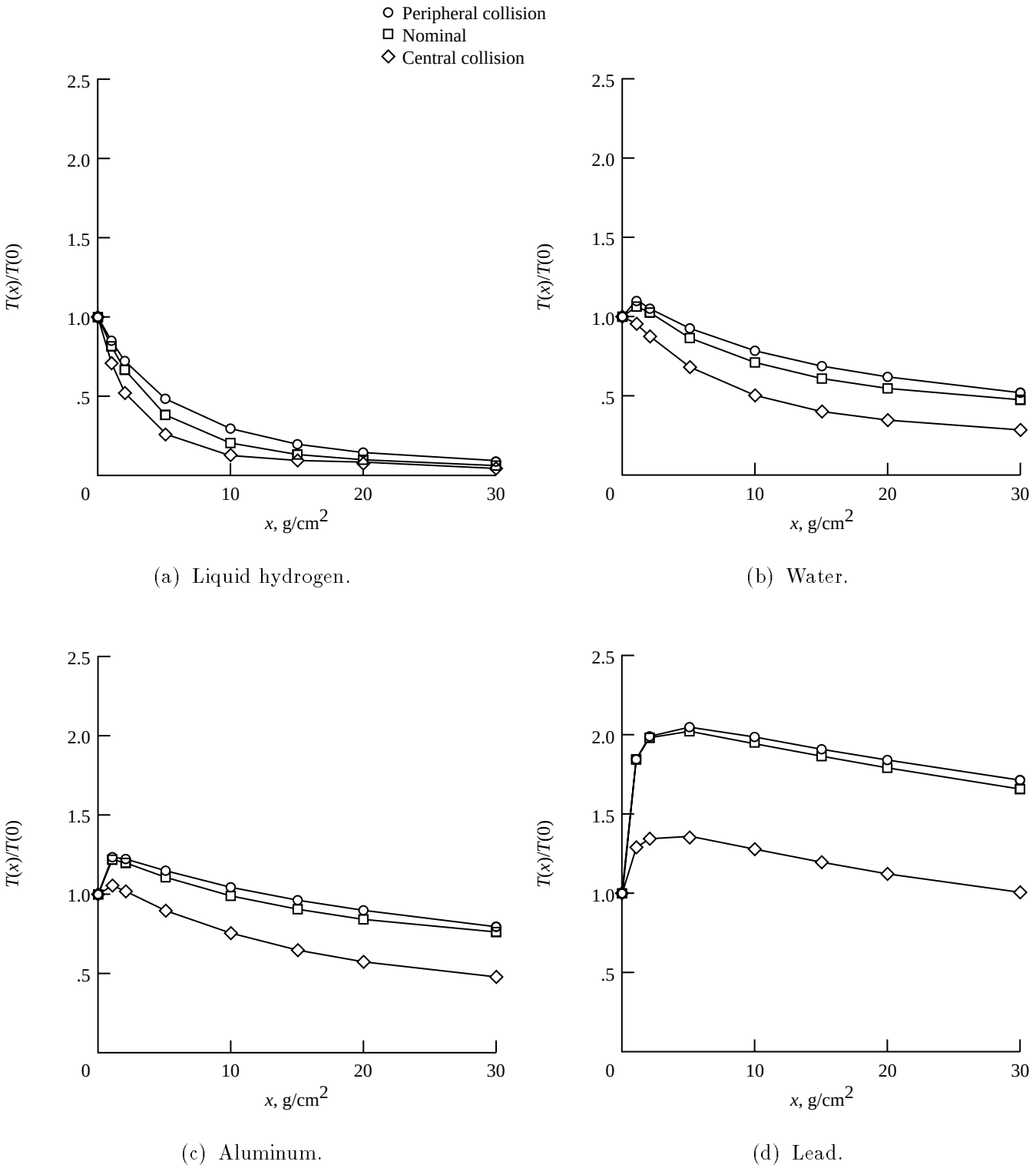

(a) Liquid hydrogen.

(b) Water.

(c) Aluminum.

(d) Lead.

Figure 16. Effects of physical limits on several shield types.

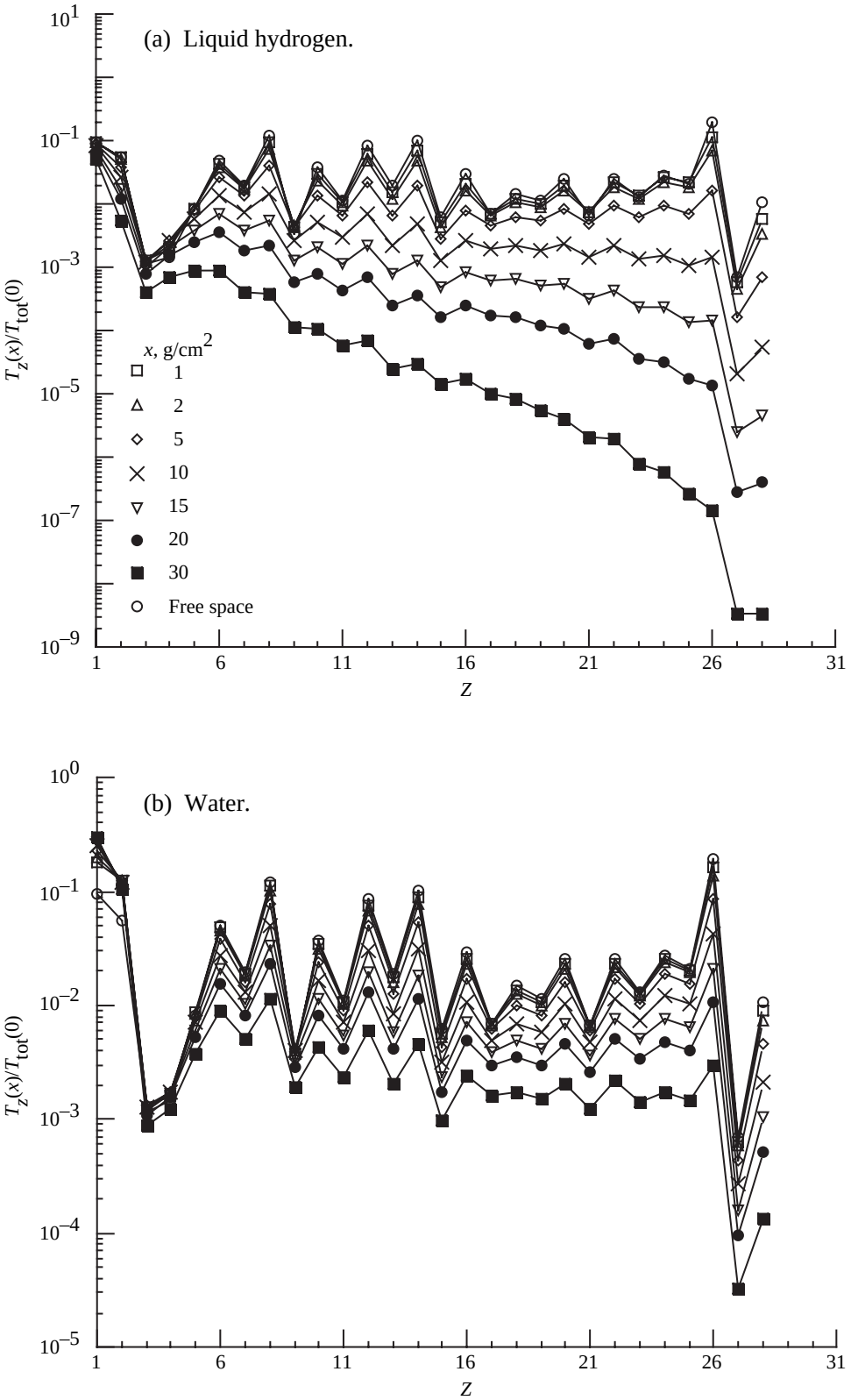

Figure 17. Contributions of biological change from each charge group of environment.

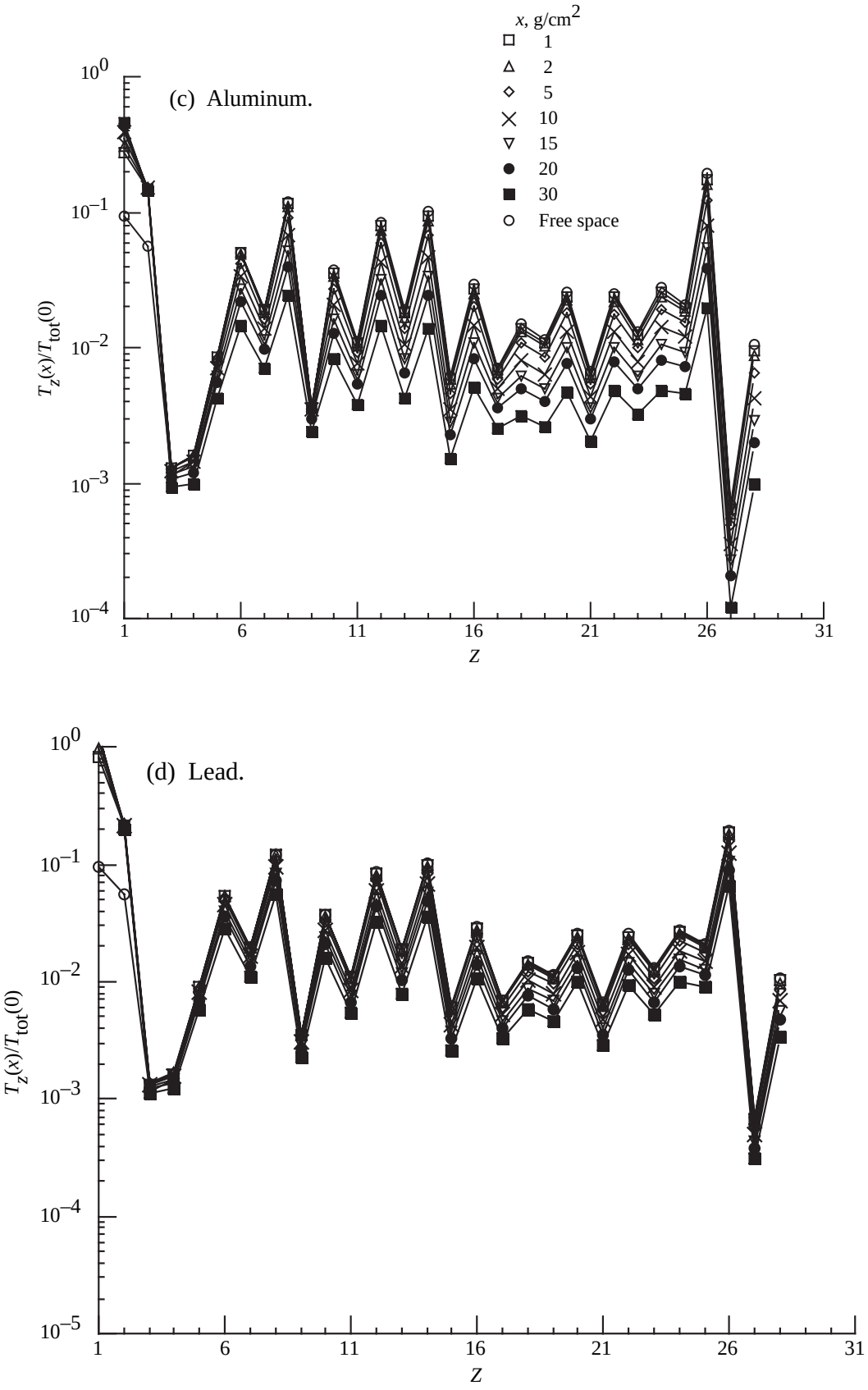

Figure 17. Concluded.

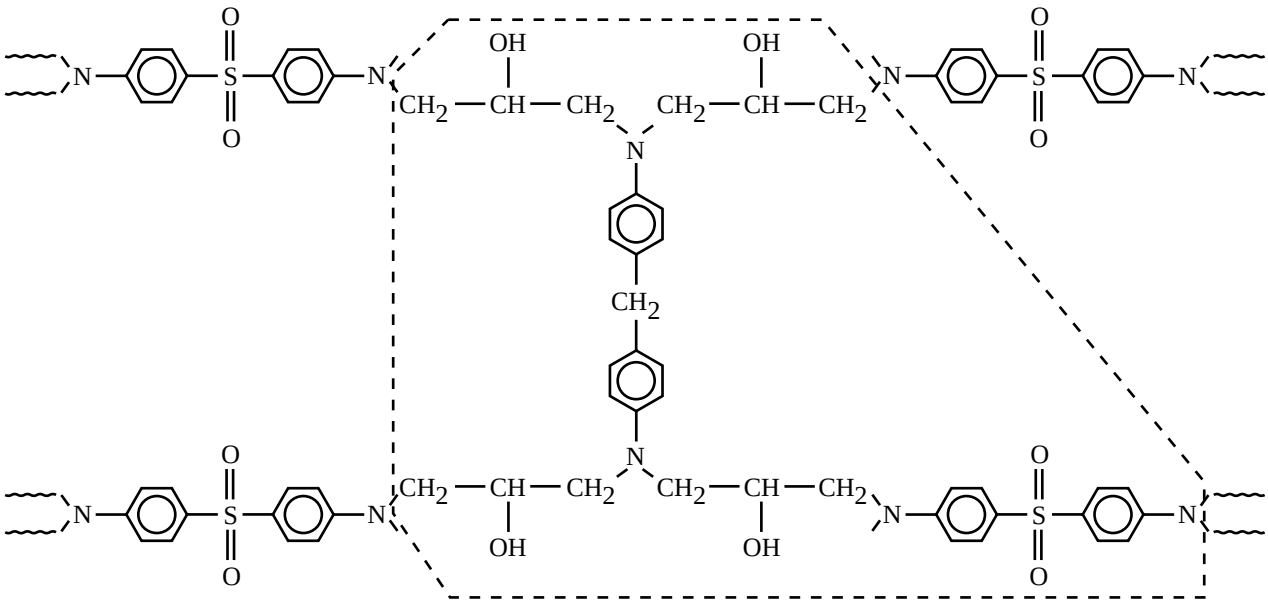

Figure 18. Tetraglycidyl $4,4'$ diamino diphenyl methane epoxy cured with diamino diphenyl sulfone.

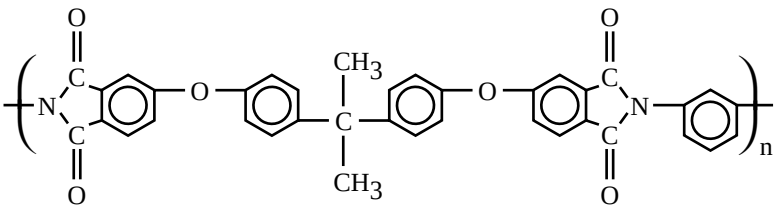

(a) Polyetherimide.

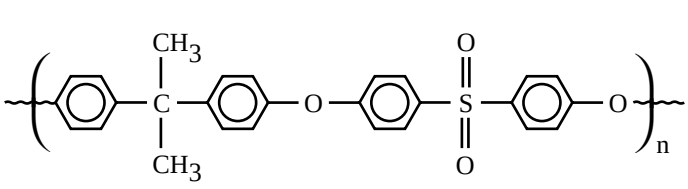

(b) Polysulfone.

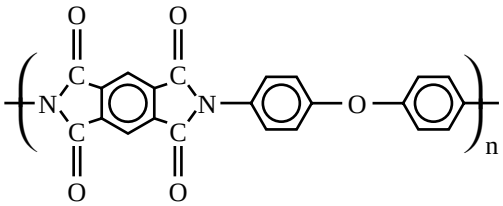

(c) Polyimide.

Figure 19. Repeat units of three polymers studied.

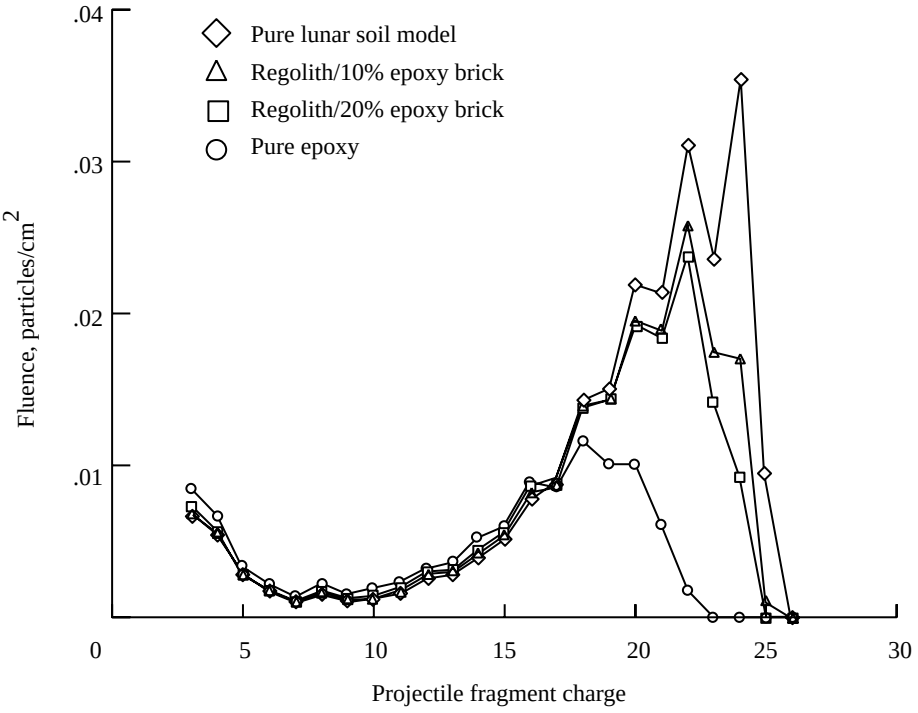

Figure 20. Attenuation of 605 MeV/amu iron beams in lunar construction materials of 16 g/cm^2 thickness.

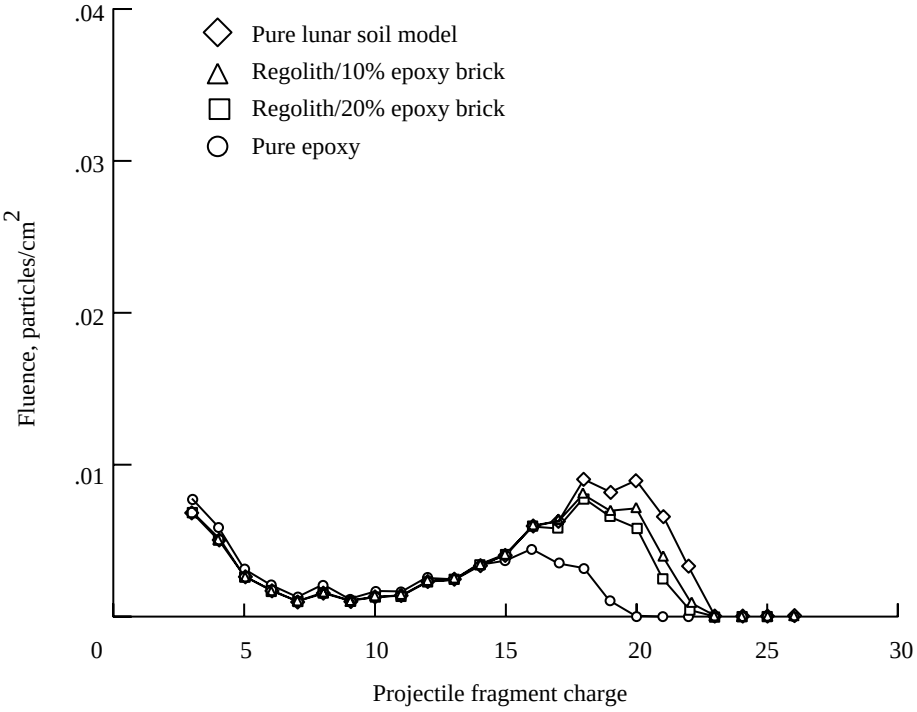

Figure 21. Attenuation of 605 MeV/amu iron beams in lunar construction materials of 18 g/cm^2 thickness.

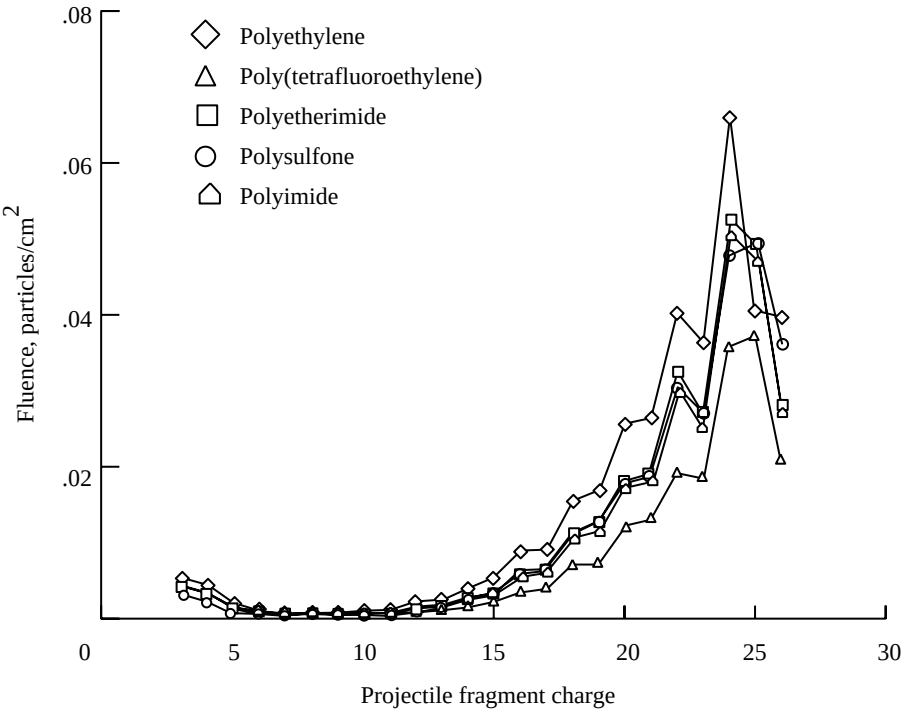

Figure 22. Attenuation of 605 MeV/amu iron beams in various polymer construction materials of 5 g/cm^2 thickness.

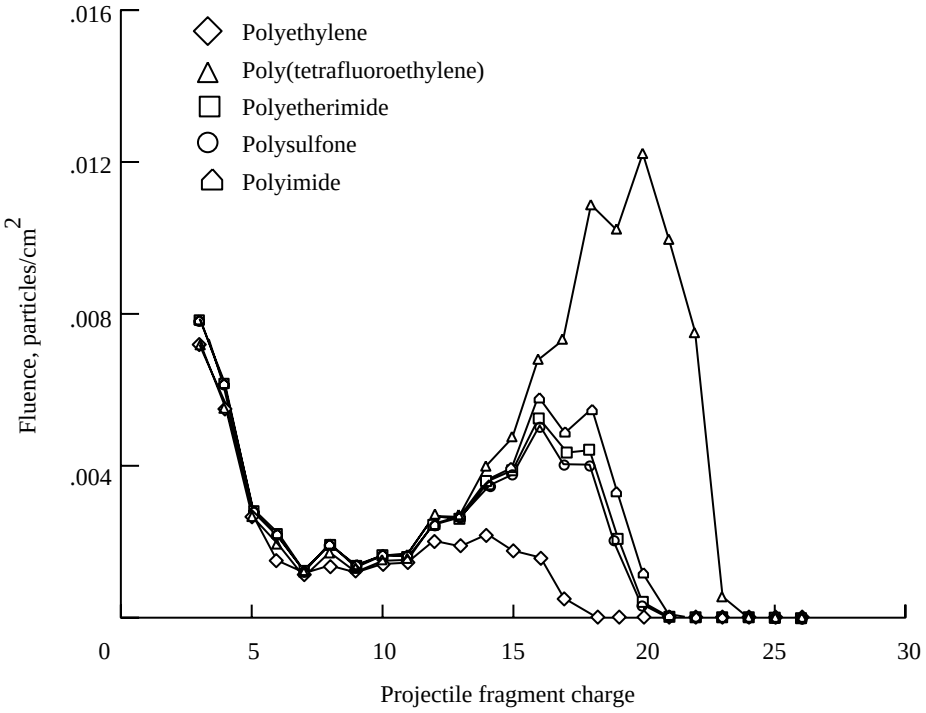

Figure 23. Attenuation of 605 MeV/amu iron beams in various polymer construction materials of 18 g/cm^2 thickness.

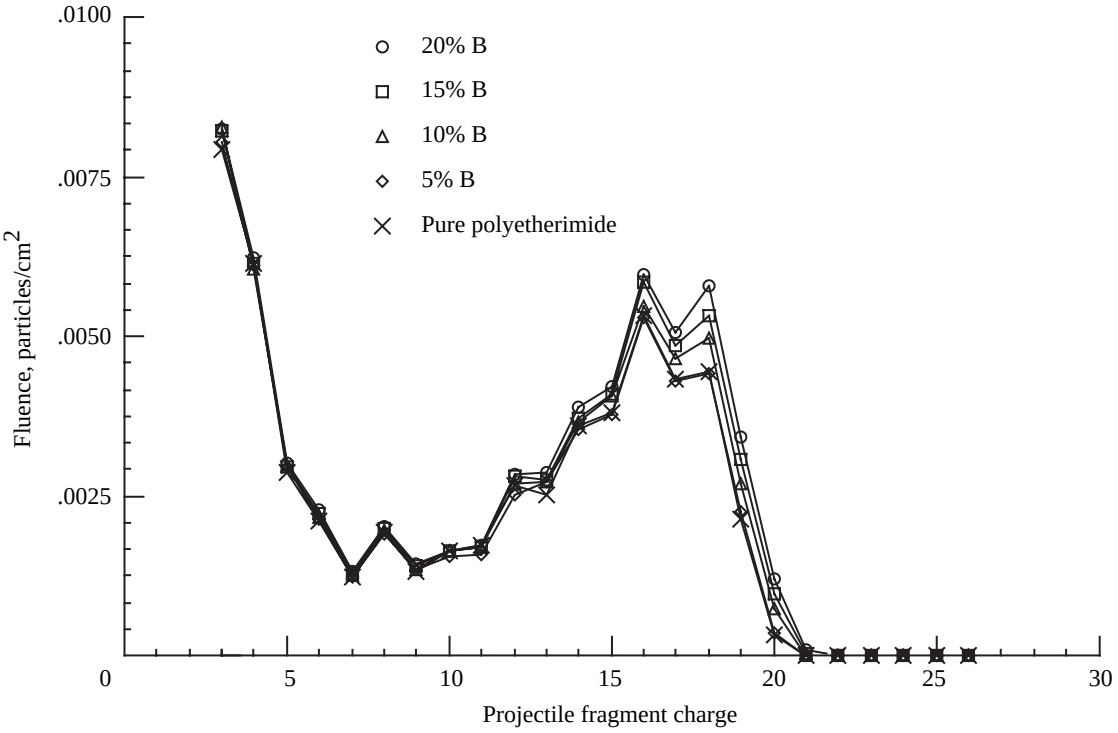

Figure 24. Attenuation of 605 MeV/amu iron beams in various weight fractions of boron-containing polyetherimide of 18 g/cm^2 thickness.

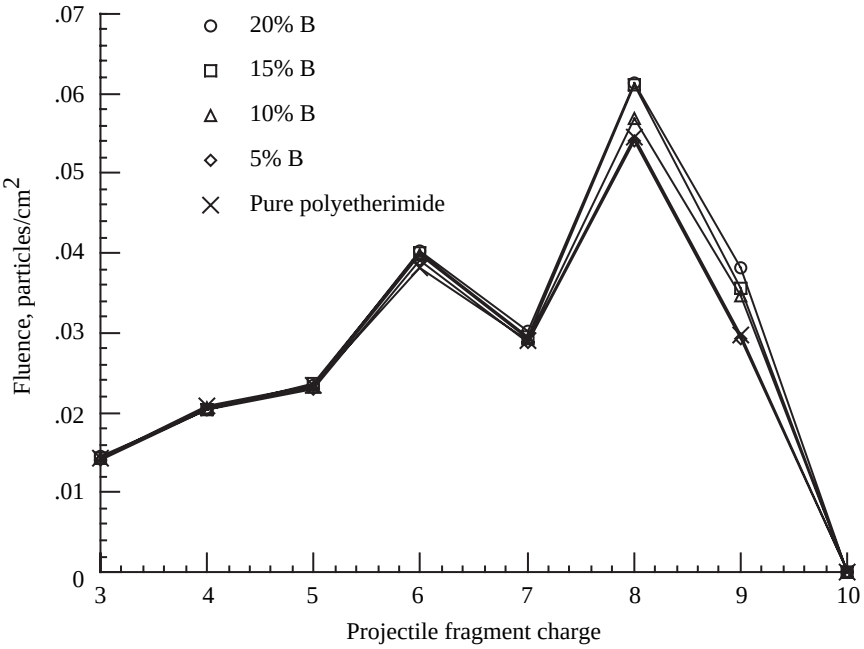

Figure 25. Attenuation of 425 MeV/amu neon beams in various weight fractions of boron-containing polyetherimide of 20 g/cm^2 thickness.

REPORT DOCUMENTATION PAGE

Form Approved
OMB No. 0704-0188

1. AGENCY USE ONLY *(Leave blank)*	2. REPORT DATE	3. REPORT TYPE AND DATES COVERED
	November 1994	Technical Paper

4. TITLE AND SUBTITLE
Performance Study of Galactic Cosmic Ray Shield Materials

5. FUNDING NUMBERS
WU 199-45-16-11

6. AUTHOR(S)
Myung-Hee Y. Kim, John W. Wilson, Sheila A. Thibeault,
John E. Nealy, Francis F. Badavi, and Richard L. Kiefer

7. PERFORMING ORGANIZATION NAME(S) AND ADDRESS(ES)
NASA Langley Research Center
Hampton, VA 23681-0001

8. PERFORMING ORGANIZATION REPORT NUMBER
L-17389

9. SPONSORING/MONITORING AGENCY NAME(S) AND ADDRESS(ES)
National Aeronautics and Space Administration
Washington, DC 20546-0001

10. SPONSORING/MONITORING AGENCY REPORT NUMBER
NASA TP-3473

11. SUPPLEMENTARY NOTES
Kim and Kiefer: College of William and Mary, Williamsburg, VA; Wilson, Thibeault, and Nealy: Langley Research Center, Hampton, VA; Badavi: Christopher Newport University, Newport News, VA.

12a. DISTRIBUTION/AVAILABILITY STATEMENT
Unclassified–Unlimited

Subject Category 93

12b. DISTRIBUTION CODE

13. ABSTRACT *(Maximum 200 words)*
The space program is faced with two difficult radiation protection issues for future long-term operations. First, retrofit of shield material or conservatism in shield design is prohibitively expensive and often impossible. Second, shielding from the cosmic heavy ions is faced with limited knowledge on the physical properties and biological responses of these radiations. The current status of space shielding technology and its impact on radiation health is discussed herein in terms of conventional protection practice and a test biological response model. The impact of biological response on the selection of optimum materials for cosmic ray shielding is presented in terms of the transmission characteristics of the shield material. Although the systematics of nuclear cross sections are able to demonstrate the relation of exposure risk to shield-material composition, the current uncertainty in nuclear cross sections will not allow an accurate evaluation of risk reduction. This paper presents a theoretical study of risk-related factors and a pilot experiment to study the effectiveness of choice of shield materials to reduce the risk in space operations.

14. SUBJECT TERMS	15. NUMBER OF PAGES
Galactic cosmic rays; Shielding; Nucleon; Biology	36
	16. PRICE CODE: A03

17. SECURITY CLASSIFICATION OF REPORT	18. SECURITY CLASSIFICATION OF THIS PAGE	19. SECURITY CLASSIFICATION OF ABSTRACT	20. LIMITATION OF ABSTRACT
Unclassified	Unclassified	Unclassified	